



# 1 **Jingwei-Nutrients: A global spatiotemporal reconstruction of ocean** 2 **nutrients (1965–2023) using multi-task deep learning**

3 Zhaokun Wang<sup>1</sup>, Bin Lu<sup>1</sup>, Yi Xin<sup>1</sup>, Takamitsu Ito<sup>2</sup>, Lei Zhou<sup>3</sup>, Lijing Cheng<sup>4</sup>, Yuanlong Li<sup>5</sup>, Xinbing Wang<sup>1</sup>, Meng Jin<sup>6</sup>

4 <sup>1</sup>School of Information Science and Electronic Engineering, Shanghai Jiao Tong University, Shanghai 200240, China

5 <sup>2</sup>School of Earth and Atmospheric Sciences, Georgia Institute of Technology, Atlanta, GA 30332, USA

6 <sup>3</sup>School of Oceanography, Shanghai Jiao Tong University, Shanghai 200030, China

7 <sup>4</sup>State Key Laboratory of Earth System Numerical Modeling and Application, Institute of Atmospheric Physics, Chinese  
8 Academy of Sciences, Beijing 100029, China

9 <sup>5</sup>Key Laboratory of Ocean Observation and Forecasting and Key Laboratory of Ocean Circulation and Waves, Institute of  
10 Oceanology, Chinese Academy of Sciences, Qingdao 266071, China

11 <sup>6</sup>School of Artificial Intelligence, Shanghai Jiao Tong University, Shanghai 200240, China

12 *Correspondence to:* Bin Lu (robinlu1209@sjtu.edu.cn), Meng Jin (jinm@sjtu.edu.cn)

13 **Abstract.** Dissolved nitrate, phosphate, and silicate are fundamental drivers of marine primary productivity and the biological  
14 carbon pump. However, the development of continuous, long-term global datasets has long been severely hindered by extreme  
15 historical data sparsity and complex biogeochemical dynamics. Statistical interpolation methods struggle to simultaneously  
16 fill the severely sparse data gaps and capture the non-linear interactions, necessitating advanced artificial intelligence (AI) to  
17 explicitly learn and leverage their underlying relationships. Nevertheless, most existing AI methods reconstruct nutrients  
18 independently (i.e., Single-Task Learning), failing to exploit the synergistic effects inherent in cross-nutrients stoichiometry.  
19 In this study, we present *Jingwei-Nutrients*, a global monthly dataset at  $1^\circ \times 1^\circ$  resolution from 0 to 2000 m depth spanning  
20 1965 to 2023, reconstructed using a Transformer-based Multi-Task Learning (MTL) framework trained on a  
21 comprehensive, quality-controlled multi-source observational database. Evaluation on the validation set yields  $R^2$  values  
22 of 0.980, 0.961, and 0.983, with RMSEs of 2.21, 0.23, and  $6.35 \mu\text{mol kg}^{-1}$  for nitrate, phosphate, and silicate, respectively.  
23 Temporal K-fold cross-validation reveals that the MTL framework consistently achieves higher  $R^2$  and lower RMSE for  
24 all three nutrients compared to single-task models, with larger accuracy gains in data-sparse earlier decades such as  
25 1965-1975. Our dataset reproduces consistent global climatology patterns and seasonal cycles with World Ocean Atlas  
26 (WOA). Furthermore, independent evaluations against long-term monitoring stations (HOT and KERFIX) and GO-SHIP  
27 cruise sections (P16N, P16S, and P06E) demonstrate our effectiveness across multi-decadal temporal trend, spatial  
28 variability and vertical changes. Additionally, an ensemble-based uncertainty analysis reveals interpretable spatial  
29 heterogeneities and a long-term decreasing trend in global uncertainty, which directly mirrors the historical transition  
30 from sparse early sampling to modern observing networks. This dataset fills a critical gap in historical ocean  
31 biogeochemical observations, providing a reliable, physically consistent foundation for marine biogeochemical modeling



32 and climate change studies. The dataset is openly available at <https://doi.org/10.5281/zenodo.19491198> (Wang et al.,  
33 2026).

## 34 **1 Introduction**

35 Nutrients—specifically nitrate, phosphate, and silicate—serve as the fundamental basis for marine ecosystems and function as  
36 critical drivers of ocean biogeochemistry (Sigman and Hain, 2012; Moore et al., 2013). Nitrate is often the proximate limiting  
37 nutrient in much of the low-latitude surface ocean, directly constraining phytoplankton growth and ecosystem productivity  
38 (Moore et al., 2013; Browning and Moore, 2023). Phosphate, while also a limiting factor in specific regions, plays a distinct  
39 role in regulating long-term ocean fertility and metabolic processes over geological timescales (Deutsch and Weber, 2012).  
40 Silicate is essential for diatoms—a key phytoplankton group responsible for a large fraction of carbon export—thereby  
41 controlling the efficiency of the biological pump and the sequestration of atmospheric CO<sub>2</sub> (Benitez-Nelson et al., 2007;  
42 Tréguer et al., 2018). Collectively, the availability and concentrations of these dissolved inorganic nutrients determine the  
43 magnitude of primary and new production across the global ocean (Lipschultz et al., 2002).

44 Although these nutrients serve distinct ecological and biogeochemical roles, they do not operate in isolation. Because these  
45 nutrients collectively fuel the biological pump, their distributions in the marine environment do not vary independently; rather,  
46 they are tightly coupled through biological uptake and regeneration processes (Deutsch and Weber, 2012). Phytoplankton  
47 consume nitrate, phosphate, and silicate in fundamentally consistent average stoichiometric proportions during photosynthesis  
48 and release them back into the water column during remineralization, establishing a robust biogeochemical linkage among  
49 their cycles (Redfield, 1934). However, contemporary syntheses reveal that rather than being rigidly static, this marine  
50 ecological stoichiometry is highly dynamic, exhibiting pronounced shifts across large-scale spatial gradients and multi-decadal  
51 timescales (Liu et al., 2025). This intrinsic, yet variable, coupling implies that the spatial and temporal distribution of one  
52 element is dynamically constrained by the others (Sarmiento and Gruber, 2006). Furthermore, the interplay between these  
53 shifting biological drivers and physical transport processes, such as water mass mixing, results in complex, non-linear  
54 hydrographic relationships that vary dynamically with depth and latitude (Ascani et al., 2013).

55 Despite their biogeochemical significance and the predictable nature of their elemental coupling, observational data for  
56 these nutrients remain limited. While physical variables such as temperature and salinity are now extensively monitored  
57 at high spatiotemporal resolution by autonomous platforms like the core Argo array (Roemmich et al., 2019), nutrient  
58 concentrations have historically been derived from discrete shipboard sampling and subsequent laboratory analysis  
59 (Olsen et al., 2016). Although the advent of the Biogeochemical-Argo (BGC-Argo) program has expanded autonomous  
60 nitrate monitoring (Claustre et al., 2020), comparable sensors for phosphate and silicate are not yet available.  
61 Consequently, the historical reliance on labor-intensive and costly ship-based operations has resulted in spatiotemporal  
62 discontinuities in the global nutrient database. Historical observations are heavily biased toward the Northern



63 Hemisphere and summer months, leaving large regions of the Southern Ocean and the deep sea poorly sampled,  
64 particularly during winter seasons (Garcia et al., 2018). Ultimately, this scarcity of continuous, four-dimensional  
65 observations hinders our ability to fully resolve the multi-scale variability of global nutrient cycles and their ecosystem  
66 responses to climate change.

67 To bridge these observational gaps and generate global nutrient fields, the oceanographic community has developed various  
68 mapping strategies over the past decades. Traditional approaches predominantly employ objective analysis or optimal  
69 interpolation techniques to map discrete nutrient profiles onto regular spatial grids (e.g., Levitus, 1982; Garcia et al., 2018).  
70 However, these statistical interpolation methods require high-density spatial coverage to maintain accuracy. Given the sparsity  
71 of historical nutrient observations, these methods are typically limited in capturing the temporal dimension, often aggregating  
72 decades of discrete sampling data to construct a single, temporally averaged background field. This spatial-temporal trade-off  
73 has led to the development of highly valuable but static climatological products, most notably the World Ocean Atlas (WOA)  
74 (Garcia et al., 2018, 2024a). Consequently, while such gridded climatologies provide a crucial baseline for the oceanic mean  
75 state, they lost temporal variance and multi-decadal biogeochemical trends, rendering them insufficient for resolving  
76 continuous, long-term global nutrient variability.

77 To address these limitations of statistical interpolation, machine learning (ML) algorithms have emerged as alternative tools  
78 capable of resolving complex, non-linear biogeochemical dynamics even within data-sparse regimes (Sauzède et al., 2017;  
79 Bittig et al., 2018; Ito et al., 2024; Lu et al., 2024). By leveraging empirical relationships between target biogeochemical  
80 variables and widely available physical predictors (e.g., temperature and salinity), these data-driven models can infer missing  
81 concentrations and reconstruct continuous fields. Building upon this paradigm, neural networks and ensemble methods have  
82 been validated across various oceanographic domains. For instance, they have demonstrated reliability in mapping global  
83 ocean carbon parameters and dissolved oxygen inventories (Landschützer et al., 2016; Gregor et al., 2019; Ito et al., 2017),  
84 indicating the capability of ML to capture intricate hydrographic couplings. Encouraged by these successes, several recent  
85 studies have extended ML applications specifically to macronutrient fields, producing valuable regional time-series or surface-  
86 only climatologies (Keppler et al., 2020; Broullón et al., 2021).

87 Despite these promising ML applications, a limitation persists across nearly all existing nutrient reconstruction frameworks:  
88 they rely on Single-Task Learning (STL) paradigms. In these conventional models, nitrate, phosphate, and silicate are treated  
89 as independent targets, with a separate neural network trained for each element. This isolated training process does not account  
90 for the stoichiometric coupling that governs ocean biogeochemistry (e.g., Redfield, 1934; Deutsch and Weber, 2012).  
91 Consequently, single-task models cannot mutually constrain their multi-element predictions, which can lead to physically  
92 inconsistent elemental ratios within the reconstructed fields, particularly across vast, data-sparse oceanic domains. Furthermore,  
93 STL models impose rigid data requirements, demanding exact target availability for training. For instance, if a historical  
94 observation contains valid phosphate measurements but lacks nitrate, the entire profile is discarded during the training of the  
95 nitrate model. Consequently, the valuable hydrographic context embedded in that observation cannot be utilized to inform the



96 coupled biogeochemical system. This fragmented approach leads to an underutilization of the already scarce historical data  
97 archives, further reducing the available training pool.

98 Recognizing the limitation of single-task models and the scarcity of continuous global time-series products, we design a Multi-  
99 Task Learning (MTL) framework (Kendall et al., 2018; Yu et al., 2020) based on the Transformer architecture (Vaswani et al.,  
100 2017). The idea of multi-task learning is to train a single model to tackle multiple related tasks at once, enabling progress in  
101 one task to implicitly benefit the others. This joint learning approach leverages the intrinsic biogeochemical stoichiometry  
102 among nitrate, phosphate, and silicate. By allowing data-rich targets to serve as auxiliary constraints for under-sampled  
103 variables, the MTL architecture maximizes the utility of fragmented historical observations, particularly in data-sparse eras.  
104 Employing this framework, we present *Jingwei-Nutrients*, a four-dimensional spatiotemporal dataset of global ocean nutrients  
105 spanning from 1965 to 2023 (An explanation of the name *Jingwei* will be provided in the section "The Name of *Jingwei*").  
106 Driven by quality-controlled in situ nutrient archives and hydrographic physical predictors, the product provides continuous,  
107 monthly oceanic fields at a  $1^{\circ} \times 1^{\circ}$  spatial resolution, covering the global ocean from the surface down to a depth of 2,000  
108 meters.

109 To verify the physical and biological representation of the reconstructed fields, we conduct multi-scale validations. These  
110 assessments include time-based K-fold cross-validation and comparative evaluations against single-task models to assess the  
111 performance of the MTL framework. Additionally, we conduct global climatology comparisons to evaluate large-scale spatial  
112 patterns and seasonal cycle, alongside independent verifications against long-term ecological time-series stations (HOT and  
113 KERFIX), and cross-section evaluations using GO-SHIP cruise sections (P16N, P16S, and P06E). Furthermore, we incorporate  
114 an ensemble-based spatiotemporal uncertainty analysis to quantify model variance and track the historical evolution of  
115 reconstruction uncertainties. Ultimately, the *Jingwei-Nutrients* dataset offers a physically consistent baseline for investigating  
116 multi-decadal ocean biogeochemical dynamics and ecosystem responses to global climate change.

117 To facilitate community access and dynamic data exploration, we develop a dedicated scientific web platform  
118 (<https://jingwei.acemap.info/map>). Beyond standard data distribution and visualization, this interactive platform integrates  
119 advanced analytical tools, allowing researchers to perform on-the-fly scientific computing, such as generating real-time vertical  
120 cross-sections and analyzing long-term time-series trajectories, directly supporting regional or global biogeochemical studies.

## 121 **2 Data and Methods**

### 122 **2.1 Observation Data**

123 To construct the observational targets and training features for the global nutrient reconstruction, we compile a database of  
124 historical in situ observations spanning from 1965 to 2023. The target variables—specifically dissolved inorganic nitrate,  
125 phosphate, and silicate—are harmonized from quality-controlled public archives, primarily the World Ocean Database 2018  
126 (WOD18; Boyer et al., 2018), the Global Ocean Data Analysis Project version 2 (GLODAPv2.2022; Lauvset et al., 2022), the



127 CLIVAR and Carbon Hydrographic Data Office (CCHDO; Sloyan et al., 2019), and the Biogeochemical-Argo (BGC-Argo)  
128 program (Claustre et al., 2020). For the model training features, we utilize hydrographic data sourced from the World Ocean  
129 Database 2023 (WOD23; Mishonov et al., 2024; Garcia et al., 2026) that are collocated with these nutrient samples. Because  
130 our reconstruction model relies on the physical identification of water masses, we select only data containing concurrent  
131 temperature and salinity (T/S) measurements. To avoid data redundancy across these archives, duplicate profiles were  
132 identified and removed based on their spatiotemporal coordinates and cruise identifiers. Following data harmonization,  
133 deduplication, collocation, and quality control, the final dataset comprises 5,292,697 collocated T/S profiles. These physical  
134 features are paired with target nutrient observations, yielding a total of 3,784,539 nitrate, 3,578,340 phosphate, and 2,931,998  
135 silicate measurements aggregated across the four archives. The detailed distribution of these observations per database is  
136 summarized in Table 1.

137 Table 1. Summary of nutrients and hydrographic data compiled from four major databases after quality control.

	WOD	CCHDO	GLODAPV2	BGC-Argo	Total
T/S	5,292,697	0	0	0	5,292,697
Nitrate	1,738,637	69,355	609,016	1,367,531	3,784,539
Phosphate	2,902,300	98,652	577,388	0	3,578,340
Silicate	2,252,702	73,165	606,131	0	2,931,998

138

## 139 2.2 Climatological Features

140 To provide the machine learning model with a consistent biogeochemical and physical mean state, we incorporate  
141 climatological fields from the World Ocean Atlas (WOA). We utilize a combination of the most recent available versions for  
142 different variables to ensure the highest data quality. These fields define the spatial reference grid for our study, featuring a  
143  $1^\circ \times 1^\circ$  horizontal resolution and 67 standard vertical levels (0–2000 m).

144 We select a total of six variables to characterize the background environment. Specifically, dissolved oxygen, oxygen  
145 saturation, and apparent oxygen utilization are obtained from the World Ocean Atlas 2023 (Garcia et al., 2024b). Climatologies  
146 for density and conductivity are sourced from the World Ocean Atlas 2018 (Locarnini et al., 2019; Reagan et al., 2019), while  
147 the mixed layer depth is derived from the WOA18 temperature and salinity fields (Locarnini et al., 2018; Zweng et al., 2018).  
148 These climatological inputs provide the mean state of the global ocean, serving as static "background" features for the machine  
149 learning model.



### 150 2.3 Time-Varying Hydrographic Predictors

151 For the global inference phase, we require continuous, time-varying, and historically consistent hydrographic inputs. We utilize  
152 the EN4.2.2 objective analysis dataset (Good et al., 2013), which provides monthly potential temperature and salinity fields  
153 from 1965 to 2023 at a  $1^\circ \times 1^\circ$  resolution.

154 We select EN4 as the hydrographic predictors because of its systematic bias correction. EN4 integrates quality-controlled  
155 profiles from the World Ocean Database (WOD), the Global Telecommunication System (GTSP), and the Argo array, while  
156 applying bias correction schemes (e.g., Gouretski and Reseghetti, 2010) to historical mechanical bathythermograph (MBT)  
157 and expendable bathythermograph (XBT) records. This processing reduces time-dependent instrumental biases, ensuring that  
158 the decadal trends in the input features represent physical variability rather than measurement artifacts.

159 Furthermore, the objective analysis framework of EN4 effectively bridges observational gaps, providing the spatiotemporally  
160 complete fields strictly required to drive global machine learning inferences. Because of its high fidelity in representing  
161 historical hydrographic environments, EN4 has been extensively validated as a foundational benchmark for capturing historical  
162 ocean heat storage and multi-decadal transport (Cheng et al., 2017; Zanna et al., 2019). Consequently, it is routinely employed  
163 as a highly reliable physical forcing dataset to drive large-scale data-driven biogeochemical mappings and carbon cycle  
164 reconstructions (Landschützer et al., 2016).

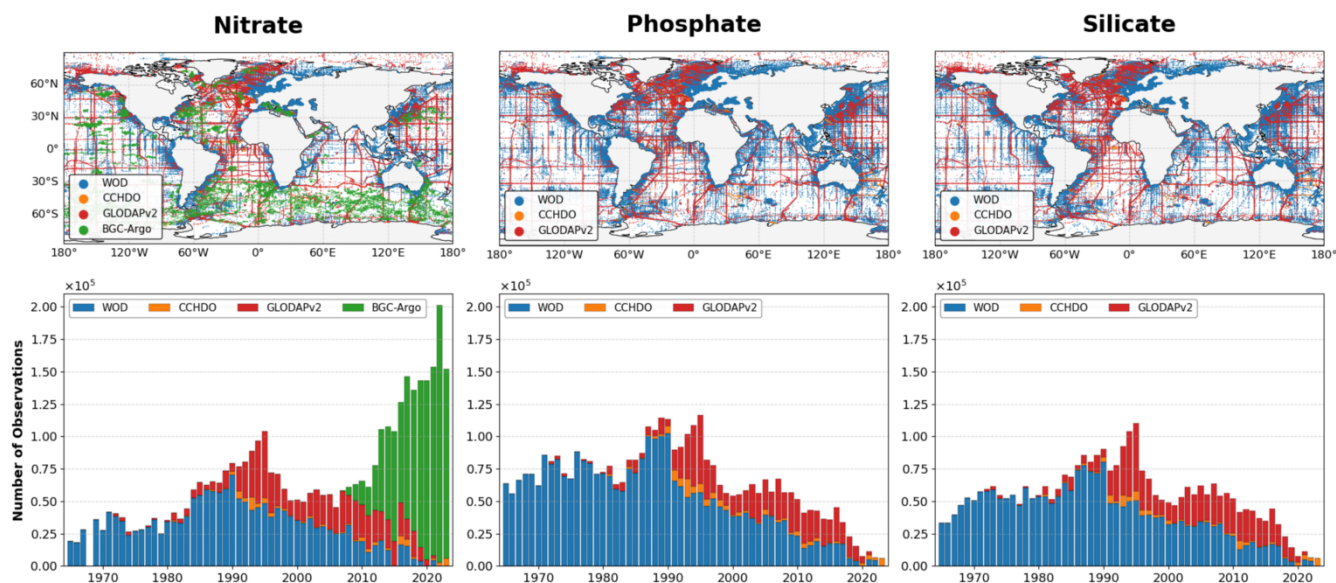
### 165 2.4 Data Quality Control

166 Because our dataset originates from diverse observational platforms and encompasses highly varied temporal and geographic  
167 scales, establishing a strict, multi-tiered quality control (QC) pipeline is critical to eliminate inaccurate records. Guided by the  
168 fundamental principles outlined in the World Ocean Database (WOD) documentation (Boyer et al., 2018), we implemented a  
169 three-stage hierarchical strategy on the merged global archive. This framework systematically filters hydrographic and nutrient  
170 variables at the measurement, station, and cruise levels.

171 The first level of our hierarchical QC protocol targets individual measurements, employing a sequence of seven specific checks  
172 to identify and remove potentially erroneous records from the combined datasets. (1) Initially, we apply a depth-specific  
173 boundary constraint optimized for our target 0–2000 m water column. By defining physically realistic domains for every  
174 variable across designated water strata, any observation exceeding these established boundaries is consequently rejected. This  
175 restriction covers temperature, salinity, and the three target nutrient parameters: nitrate ( $NO_3^-$ ), phosphate ( $PO_4^{3-}$ ), and silicate  
176 ( $Si(OH)_4$ ). (2) We evaluate the biogeochemical consistency of the data by checking empirical relationships between paired  
177 variables. We validate observations against accepted theoretical spaces for both physical pairings (T–S) and physical-  
178 biogeochemical combinations (e.g., T–N, T–P, T–Si, S–N, S–P, S–Si) to guarantee alignment with recognized water mass  
179 signatures. (3) To capture extreme statistical anomalies, we compute the local mean and standard deviation for each standard  
180 depth horizon. Any value shifting beyond six standard deviations from its respective mean is tagged as an outlier. (4) We



181 assess vertical continuity by calculating the vertical gradient for each parameter. Any measurement showing a vertical rate of  
182 change that exceeds the mean gradient by more than five standard deviations is marked as questionable. (5) A density inversion  
183 assessment targets physically improbable vertical structures. Since parameters such as temperature and nutrients typically  
184 exhibit monotonic relationships with depth or potential density ( $\sigma_\theta$ ) in stratified waters, measurements violating preset  
185 thresholds for relationships (e.g., Depth–T, Depth–Nutrient, or  $\sigma_\theta$ –Nutrient) are flagged. (6) We identify vertical spikes by  
186 comparing each measurement directly against its immediate upper and lower neighbors. If this difference exceeds a preset  
187 limit, the observation is flagged as a spike. (7) Finally, we rely on the original quality flags provided by the source databases.  
188 We only retain measurements explicitly labeled as 'good' and discard any records marked as questionable or bad.  
189 Following the assessment of individual measurements, regarding to the second level, we extend the quality control framework  
190 to the station and cruise levels to address systematic inconsistencies. To ensure vertical profile reliability, any station containing  
191 more than 30% of data points flagged during the initial screening is deemed unreliable and entirely discarded. Similarly, at the  
192 expedition level, cruises exhibiting an aggregate flag rate exceeding 40% are excluded to prevent the propagation of systematic  
193 instrumental errors or calibration drifts. The final selection process integrates flags across this hierarchy, permanently  
194 removing any data identified as erroneous at the individual, station, or cruise stage.  
195 The final level of our quality control protocol is specifically designed to align with the input-output structure of the multi-task  
196 learning framework. Since the reconstruction relies on physical predictors to infer biogeochemical fields, complete availability  
197 of temperature and salinity is mandatory. Therefore, we apply a strict filter to ensure that every retained nutrient observation  
198 is strictly collocated with valid, high-quality physical measurements (T and S). However, unlike single-task models that might  
199 require simultaneous observations of all target variables, our multi-task architecture allows for valid training with partial targets.  
200 To maximize data utilization, we do not require the concurrent presence of all three nutrients. Instead, any data point containing  
201 valid physical predictors and at least one valid nutrient measurement is retained. This flexible inclusion strategy allows the  
202 model to leverage a significantly larger volume of historical data—where specific nutrients might be missing—thereby  
203 enhancing the distinct feature extraction capability for each element. This inclusion strategy maximizes the volume of historical  
204 data available for training. The resulting high-quality dataset exhibits extensive global coverage spanning the period 1965–  
205 2023, with the specific spatiotemporal distribution patterns illustrated in Fig. 1.



206  
207

Figure 1. Spatial and temporal distribution of the nutrients data after quality control.

## 208 2.5 Model development and Validation

### 209 2.5.1 Input Features

210 The selection of input features is designed to constrain the machine learning model with both physical principles and statistical  
211 priors. The input vector consists of three distinct categories: encoded spatiotemporal coordinates, hydrographic predictors, and  
212 climatological reference features. To preserve the continuity of the global domain and the cyclical nature of seasonality, we  
213 apply specific feature engineering techniques: spatial coordinates are transformed into spherical coordinates, and the month  
214 variable is encoded into sine and cosine components to capture the continuous seasonal cycles. A list of all input variables,  
215 along with their respective sources and resolutions, is summarized in Table 2.

216 Potential temperature and salinity are selected as the primary physical drivers based on the fundamental control of water mass  
217 dynamics on nutrient distributions. Oceanographic studies have long established that nutrient concentrations exhibit distinct  
218 relationships with temperature and salinity along isopycnal surfaces, enabling these hydrographic variables to serve as effective  
219 proxies for identifying distinct water masses. Consequently, utilizing collocated temperature and salinity as core predictors  
220 has become a standard practice in global biogeochemical reconstruction models (e.g., Sauzède et al., 2017; Bittig et al., 2018;  
221 Broullón et al., 2019; Keppler et al., 2020; Carter et al., 2021).

222 Furthermore, we incorporate six climatological variables from WOA to serve as spatial reference features. By explicitly  
223 including these mean environmental states as inputs, the neural network is guided to learn the non-linear relationships between  
224 the background hydrographic conditions and nutrient distributions. This "climatology-informed" strategy provides a stable  
225 environmental reference baseline, enhancing model stability and convergence.



226 To align the model inputs with observational reality, we implement a distinct data construction strategy for the training and  
 227 inference phases. During the training phase, the model inputs are derived from the quality-controlled observational dataset to  
 228 represent in situ conditions. Specifically, we use the in situ measured temperature and salinity, while the corresponding  
 229 climatological features are obtained by linearly interpolating the standard WOA grids to the exact spatiotemporal position of  
 230 each nutrient observation. In contrast, the global inference phase requires spatially continuous products to generate the full 4D  
 231 reconstruction. Drawing on its established role as a robust physical forcing in historical oceanographic reconstructions (Cheng  
 232 et al., 2017; Zanna et al., 2019) and large-scale biogeochemical mappings (Landschützer et al., 2016), we directly utilize the  
 233 time-varying EN4 gridded fields to represent the historical hydrographic conditions. Concurrently, the WOA climatological  
 234 features are drawn directly from their standard grid points. This dual strategy ensures that the model is trained on local  
 235 relationships while being capable of projecting these learned patterns onto the global domain driven by spatiotemporal physical  
 236 inputs.

237 Table 2. Summary of the input variables used for the global nutrient reconstruction, including their respective data sources, temporal  
 238 coverage, and spatial resolutions.

Feature name	Data source	Spatial resolution	Temporal resolution
<i>Geographical features</i>			
Latitude [° N]	Sampling information		
Longitude [° E]	Sampling information		
Depth [m]	Sampling information		
<i>Oceanographic features</i>			
Temperature [°C]	World Ocean Database 2023		
Salinity [unitless]	World Ocean Database 2023		
Dissolved oxygen [ $\mu\text{mol kg}^{-1}$ ]	World Ocean Atlas 2023	$1^\circ \times 1^\circ$	Annual climatology
Percent Oxygen Saturation [%]	World Ocean Atlas 2023	$1^\circ \times 1^\circ$	Annual climatology
Apparent Oxygen Utilization [ $\mu\text{mol kg}^{-1}$ ]	World Ocean Atlas 2023	$1^\circ \times 1^\circ$	Annual climatology
Density [ $\text{kg/m}^3$ ]	World Ocean Atlas 2018	$1^\circ \times 1^\circ$	Seasonal climatology
Conductivity [S/m]	World Ocean Atlas 2018	$1^\circ \times 1^\circ$	Seasonal climatology
Mixed Layer Depth [m]	World Ocean Atlas 2018	$1^\circ \times 1^\circ$	Monthly climatology

239

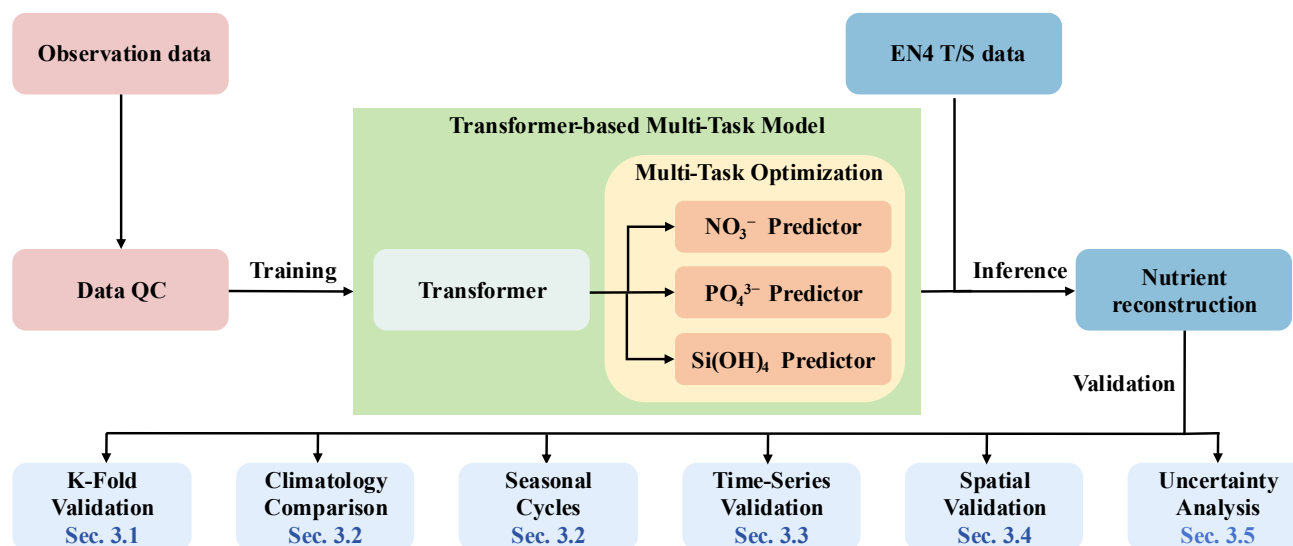
## 240 2.5.2 Model Architecture

241 The operational workflow detailing the training and inference phases of the *Jingwei-Nutrients* model is illustrated in Fig. 2. At  
 242 the core of this pipeline, to capture the complex, non-linear interactions between physical drivers and biogeochemical tracers,  
 243 we employ a Transformer-based deep learning architecture. This framework, originally developed for natural language



244 processing (Vaswani et al., 2017), has been recently adapted for high-dimensional Earth system modeling (e.g., Bi et al., 2023;  
245 Lam et al., 2023) and complex oceanographic field reconstructions (Reichstein et al., 2019; Sonnewald et al., 2021). The  
246 cornerstone of this architecture is the self-attention mechanism, which fundamentally distinguishes it from traditional  
247 regression models or standard convolutional networks.

248 Unlike static methods that treat input features independently, the self-attention mechanism dynamically calculates "attention  
249 weights" to quantify the relevance of different input features relative to one another. In the context of nutrient reconstruction,  
250 this capability allows the model to inherently learn and weigh the variable coupling strength between specific physical  
251 conditions (e.g., temperature, salinity, depth) and nutrient concentrations. By establishing these adaptive connections, the  
252 Transformer can focus on the most critical predictors for identifying distinct water masses, thereby improving prediction  
253 accuracy in spatially heterogeneous ocean environments.



254 **Figure 2.** The overall pipeline of the *Jingwei-Nutrients* reconstruction framework, encompassing data preparation, the Transformer-based  
255 MTL neural network architecture, global 4D inference, and comprehensive performance validation.

256 Specifically, the network architecture adopts a Multi-Task Learning (MTL) framework designed to simultaneously reconstruct  
257 the three target nutrients ( $NO_3^-$ ,  $PO_4^{3-}$ , and  $Si(OH)_4$ ). The network is composed of a shared feature extraction backbone followed  
258 by three element-specific prediction heads. The input feature vector is initially processed by shared Transformer encoder layers,  
259 which are designed to capture the coupled physical-biogeochemical linkages driven by the hydrographic environment. Rather  
260 than learning isolated generic representations, these shared layers extract the concurrent stoichiometric relationships among  
261 the nutrients. Subsequently, the shared feature representations are routed into three parallel, task-specific decoding heads. Each  
262 head acts as a specialized regression module dedicated to a single element, optimizing for its unique vertical gradient and  
263 spatial distribution. Crucially, during training, the specific biogeochemical constraints from each decoding head are  
264 continuously propagated back to the shared layers. By mutually constraining the shared representation space, the MTL



265 framework enables the joint learning of coherent biogeochemical patterns. This dynamic mutual calibration not only enhances  
266 computational efficiency through shared weights but, more importantly, provides a structural mechanism to encourage  
267 stoichiometric consistency. By sharing representations across elements, the model is inherently guided to learn their concurrent  
268 biogeochemical variations, reducing the likelihood of generating the physically divergent patterns that can arise from training  
269 independent single-task models.

### 270 2.5.3 Multi-Task Optimization Strategy

271 The stoichiometric ratios among marine nutrients are not globally static; rather, they exhibit pronounced variability across  
272 distinct horizontal domains, depth horizons, and temporal scales (Liu et al., 2025). Consequently, imposing rigid empirical  
273 constraints, such as the classical Redfield ratio, is insufficient for capturing the complex reality of global biogeochemical  
274 cycles. To address this, we employ a data-driven multi-task learning approach, enabling the neural network to autonomously  
275 infer and represent these dynamic elemental relationships within its shared latent space.

276 However, while this multi-task architecture enables flexible information sharing without hard-coded rules, the joint training  
277 process introduces two fundamental optimization challenges: loss scale imbalance and gradient conflict. If simply summed  
278 with equal weights, tasks with larger loss magnitudes can dominate the optimization process, while conflicting gradient  
279 directions between tasks can lead to "negative transfer" (Yu et al., 2020; Vandenhende et al., 2022), where improving the  
280 prediction of one nutrient degrades the performance of others. To address these issues and ensure balanced convergence across  
281 all biogeochemical variables, we implement a dual-strategy optimization framework.

282 To strictly address the optimization imbalance caused by differing variances and units among  $NO_3^-$ ,  $PO_4^{3-}$ , and  $Si(OH)_4$ , we  
283 implement an adaptive weighting scheme based on homoscedastic uncertainty (Kendall et al., 2018). Instead of manually  
284 assigning fixed hyperparameters, this method treats the task-dependent weight as a learnable parameter derived from the  
285 inherent observation noise. The total multi-task objective function  $L_{total}$  is formulated as Eq. (1):

$$286 \mathcal{L}_{total}(W, \sigma_1, \dots, \sigma_T) = \sum_{t \in \{N, P, Si\}} \left( \frac{1}{2\sigma_t^2} \mathcal{L}_t(W) + \log \sigma_t \right), \quad (1)$$

287 where  $L_t(W)$  denotes the task-specific loss (MSE) for nutrient  $t$ , and  $\sigma_t$  represents the learnable noise parameter. In Eq. (1), the  
288 term  $\frac{1}{2\sigma_t^2}$  automatically down-weights tasks with high uncertainty, while the regularization term  $\log \sigma_t$  prevents the variance  
289 from increasing indefinitely, allowing the model to dynamically balance the learning focus among the three elements  
290 throughout the training process.

291 Furthermore, to mitigate the geometric conflicts where the gradient update for one task might detrimentally affect another, we  
292 integrate the Project Conflicting Gradients (PCGrad) algorithm (Yu et al., 2020). This strategy monitors the cosine similarity



293 between the gradient vectors of any two tasks during backpropagation. When a conflict is detected (i.e., their dot product is  
294 negative), the gradient is projected to eliminate the destructive component, as calculated in Eq. (2):

$$295 \quad g_i^{PC} = g_i - \frac{g_i \cdot g_j}{\|g_j\|^2} g_j, \quad (2)$$

296 where  $g_i$  and  $g_j$  denote the original gradient vectors for task  $i$  and task  $j$ , respectively, and  $g_i^{PC}$  represents the corrected gradient  
297 for task  $i$  projected onto the normal plane of  $g_j$ . By iteratively applying this projection, PCGrad ensures that the optimization  
298 trajectory remains on a "constructive" manifold where all tasks can improve simultaneously, effectively eliminating the risk  
299 of negative transfer between nutrient species.

#### 300 2.5.4 Model Evaluation and Experimental Design

301 The reconstruction performance is quantitatively evaluated using two standard statistical metrics: the Coefficient of  
302 Determination ( $R^2$ ) and Root Mean Square Error (RMSE). Let  $N$  denote the total number of matched samples, while  $y_{obs,i}$  and  
303  $y_{pred,i}$  represent the observed and predicted values for the  $i$ -th sample, respectively, and  $\bar{y}_{obs}$  is the mean of the observed values.  
304 These metrics are calculated as follows:

$$305 \quad R^2 = 1 - \frac{\sum_{i=1}^N (y_{obs,i} - y_{pred,i})^2}{\sum_{i=1}^N (y_{obs,i} - \bar{y}_{obs})^2}, \quad (3)$$

$$306 \quad RMSE = \sqrt{\frac{1}{N} \sum_{i=1}^N (y_{obs,i} - y_{pred,i})^2}, \quad (4)$$

307 To evaluate the model's performance and the effects of the proposed architecture, we design a rigorous training and  
308 comparative framework. We adopt a strict time-based K-fold cross-validation strategy to prevent temporal data leakage. By  
309 partitioning the 59-year dataset into chronological blocks rather than random subsets, distinct time periods are rigorously  
310 isolated as test sets, providing an objective assessment of the model's generalization. Within this cross-validation framework,  
311 we further establish a comparative baseline by training independent Single-Task Learning (STL) models for each nutrient.  
312 Comparing the proposed multi-task framework against these single-element counterparts under identical conditions allows us  
313 to verify the mutual enhancement effects driven by shared feature learning.

314 Beyond statistical benchmarks, a multi-dimensional verification scheme is implemented to assess the physical and  
315 biogeochemical representation of the reconstruction. This comprehensive evaluation includes: (1) Climatological Patterns and  
316 Seasonal Cycles, which examines the reproduction of large-scale seasonal variations and long-term trends; (2) Temporal  
317 Dynamics through Station Validation, where representative stations are selected to evaluate the time-series dynamics and  
318 vertical profiles; (3) Spatial Variability through Cruise Verification, utilizing independent cruise data to assess the spatial

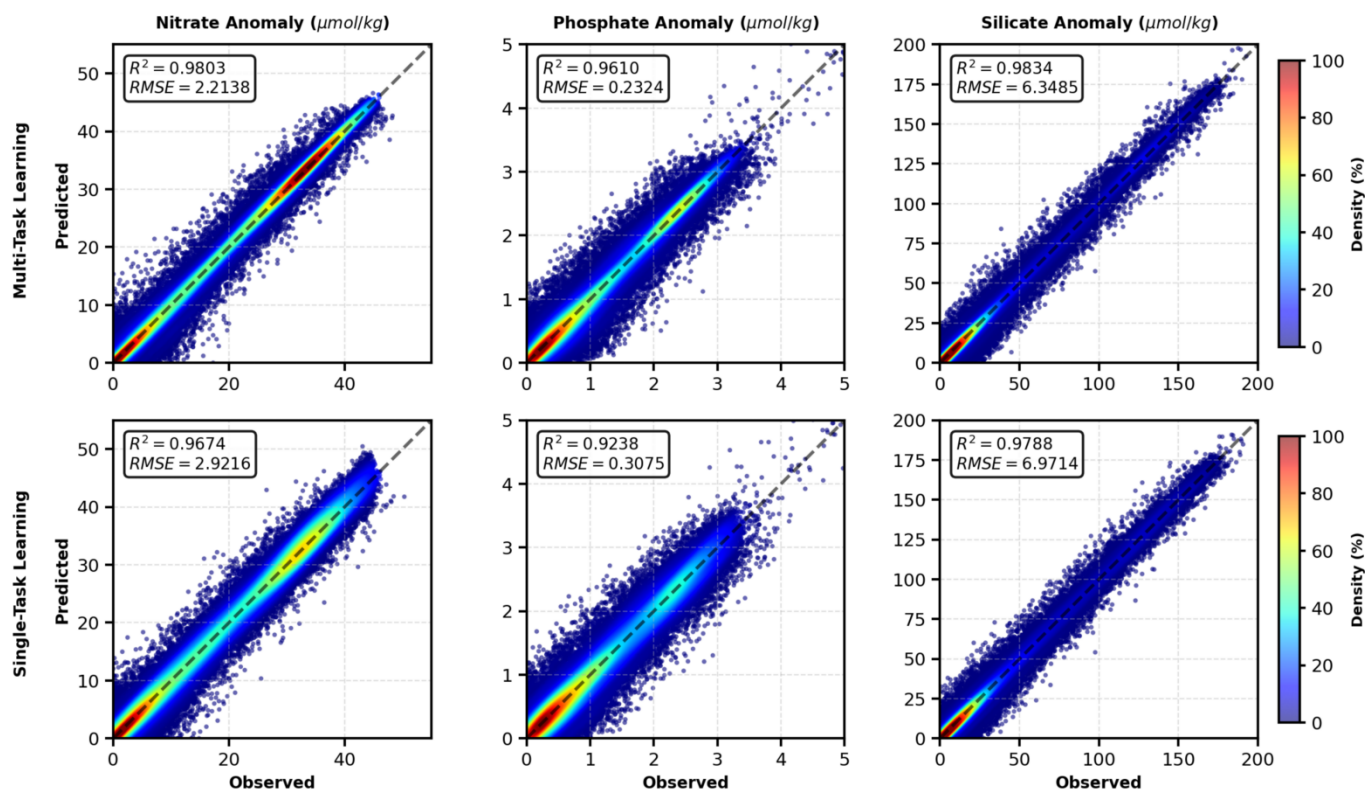


319 representation of nutrient distributions across ocean basins; and (4) Spatiotemporal Uncertainty Analysis, which quantifies the  
320 model variance and uncertainties of the reconstructed dataset across different oceanic regions and historical periods. Detailed  
321 results and analyses from these validation modules are presented in Section 3.

## 322 **3 Results**

### 323 **3.1 Model Performance**

324 The reconstruction performance of the proposed Multi-Task Learning (MTL) and Single-Task Learning (STL) models is  
325 evaluated using aggregated predictions from the validation sets of the time-based K-fold cross-validation. Figure 3 presents  
326 the density scatter plots comparing the reconstructed nutrient concentrations against the in situ observations across the full  
327 study period (1965–2023) for both architectures. By utilizing chronological blocking rather than random partitioning, the  
328 evaluation mitigates the influence of short-term temporal persistence, providing an objective assessment of the models'  
329 generalization capabilities. The scatter distributions for both the MTL and STL models generally align with the 1:1 reference  
330 line across the concentration spectrum, indicating that the models can reproduce the concentration limits without systematic  
331 bias. Furthermore, a comparison of the scatter distributions reveals that the MTL model shows tighter alignment with the  
332 reference line than the STL model, demonstrating improved reconstruction performance for all three nutrients.



333 **Figure 3.** Density scatter plots comparing the *Jingwei-Nutrients* reconstructed concentrations against in situ observations for nitrate,  
334 phosphate, and silicate. The plots aggregate all matched test samples from the strict time-based K-fold cross-validation over the entire study  
335 period (1965–2023). Colors indicate the density of data points, and the dashed line represents the 1:1 ideal agreement.

336 Table 3 summarizes the quantitative metrics ( $R^2$  and RMSE) to further assess the specific effects of the multi-task architecture  
337 compared to the single-task baselines. On average, the MTL framework yields  $R^2$  values of 0.9803, 0.9610, and 0.9834 for  
338 nitrate, phosphate, and silicate, respectively, with corresponding mean RMSE values of 2.2138, 0.2324, and 6.3485. As shown  
339 in Table 3, the joint learning framework consistently yields lower RMSE and higher  $R^2$  values compared to the single-element  
340 models across all chronological folds. Overall, the MTL approach reduces the fold-averaged RMSE by approximately 24.2%  
341 for nitrate and 24.4% for phosphate compared to their STL counterparts, along with an 8.9% reduction for silicate. This  
342 improvement can be attributed to the shared representation mechanism of the MTL architecture. By processing the elements  
343 jointly, the model is guided to learn their concurrent biogeochemical variations, which contributes to the observed  
344 improvements in numerical accuracy compared to the isolated single-task models.

345 Beyond the performance differences between the two architectures, a common characteristic observed in both the MTL and  
346 STL results is a progressive improvement in predictive performance from the 1960s to the 2020s. For instance, the MTL RMSE  
347 for nitrate is decreased from 2.9643 in the 1965–1975 fold to 1.3193 in the 2016–2023 fold. This temporal trend corresponds  
348 with the historical evolution of global ocean observing systems; the relatively higher errors in earlier decades relate to the



349 spatial sparsity of historical bottle measurements, whereas recent accuracy gains reflect the availability of high-density  
 350 hydrographic observations that provide additional physical constraints for the models.

351 Table 3. Statistical evaluation metrics ( $R^2$  and RMSE) of the chronological K-fold cross-validation. The results highlight the decadal  
 352 performance evolution and compare the predictive accuracy of the MTL architecture against independent STL models for nitrate,  
 353 phosphate, and silicate reconstructions. The unit for all RMSE values is  $\mu\text{mol kg}^{-1}$ .

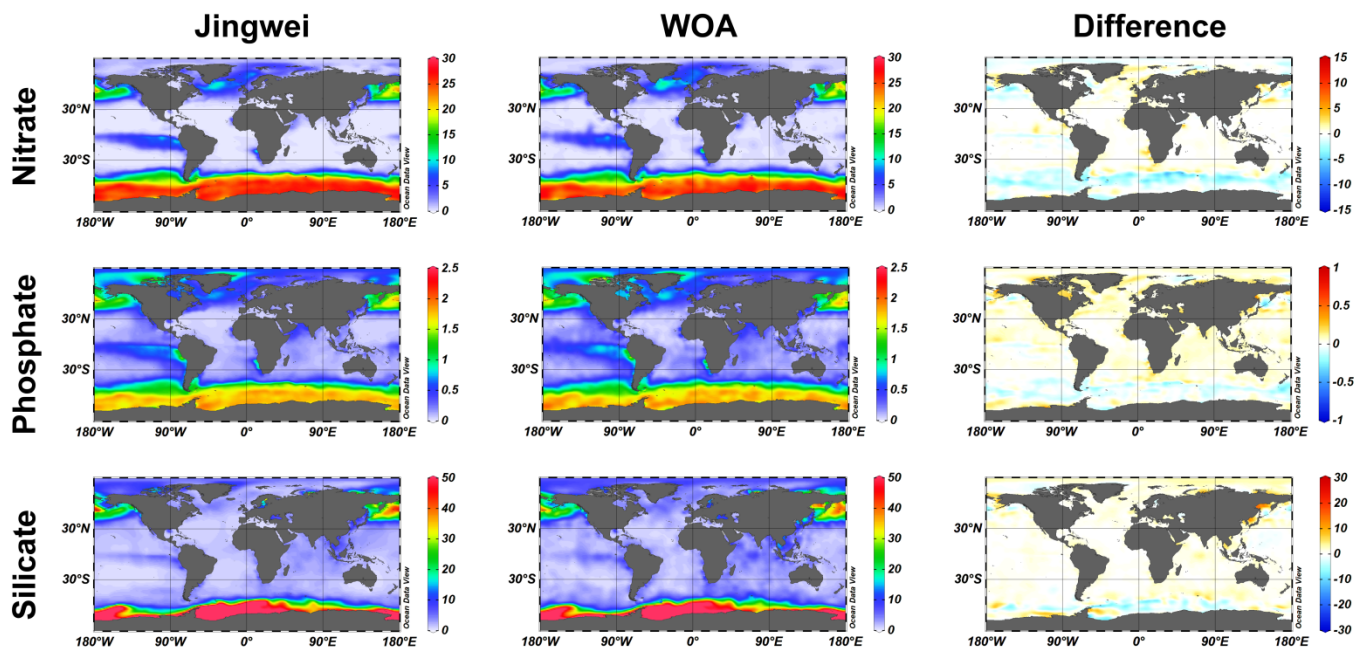
Fold	Multi-Task Learning						Single-Task Learning					
	N ( $R^2$ /RMSE)		P ( $R^2$ /RMSE)		Si ( $R^2$ /RMSE)		N ( $R^2$ /RMSE)		P ( $R^2$ /RMSE)		Si ( $R^2$ /RMSE)	
1965-1975	0.9661	2.9643	0.9339	0.3157	0.9651	8.3556	0.9532	3.9120	0.8967	0.4177	0.9605	9.1755
1976-1985	0.9701	2.7613	0.9280	0.3084	0.9718	8.0540	0.9572	3.6442	0.8908	0.4080	0.9672	8.8442
1986-1995	0.9754	2.4478	0.9518	0.2545	0.9799	7.0383	0.9625	3.2304	0.9146	0.3368	0.9753	7.7289
1996-2005	0.9860	2.0081	0.9787	0.1954	0.9929	5.3647	0.9731	2.6501	0.9415	0.2586	0.9883	5.8910
2006-2015	0.9900	1.7820	0.9827	0.1809	0.9946	4.8421	0.9771	2.3517	0.9455	0.2394	0.9900	5.3172
2016-2023	0.9942	1.3193	0.9909	0.1395	0.9961	4.4363	0.9813	1.7412	0.9537	0.1845	0.9915	4.8716
Avg	0.9803	2.2138	0.9610	0.2324	0.9834	6.3485	0.9674	2.9216	0.9238	0.3075	0.9788	6.9714

354

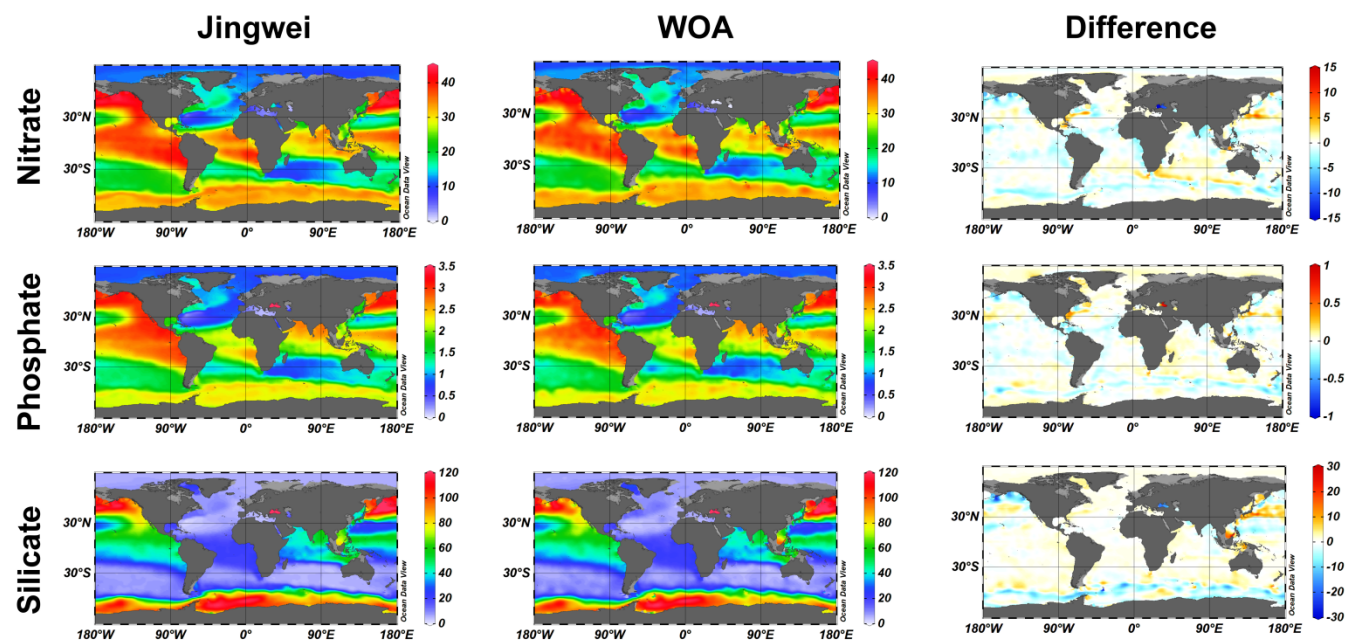
### 355 3.2 Climatological Patterns and Seasonal Cycles

356 To evaluate whether the *Jingwei-Nutrients* dataset captures the fundamental biogeochemical structure of the global ocean, we  
 357 compare the model-derived climatologies with the standard World Ocean Atlas 2023 (WOA23). This comparison assesses  
 358 whether the *Jingwei-Nutrients* model captures large-scale spatial patterns rather than overfitting to local observations. Figures  
 359 4 to 6 display the comparison of spatial distributions for nitrate, phosphate, and silicate across three representative depth layers:  
 360 the surface (0 m), the intermediate layer (500 m), and the deep layer (2000 m). Overall, the reconstructed fields show spatial  
 361 agreement with WOA23, reproducing the major global nutrient regimes across these selected depths.

362 The spatial patterns at each evaluated stratum reflect distinct physical-biogeochemical dynamics. As illustrated in Fig. 4, at  
 363 the surface layer (0 m), the model reproduces the global nutrient regimes governed by biological uptake and physical  
 364 stratification, identifying the nutrient-depleted oligotrophic subtropical gyres alongside the High-Nutrient Low-Chlorophyll  
 365 (HNLC) outcropping in the Southern Ocean (Moore et al., 2013). At the intermediate layer (500 m) in Fig. 5, the spatial  
 366 patterns transition to reflect organic matter remineralization and main thermocline ventilation, mapping the accumulation of  
 367 regenerated nutrients in the North Pacific and Indian Ocean oxygen minimum zones (OMZs) (Paulmier and Ruiz-Pino, 2009;  
 368 Sarmiento and Gruber, 2006). In the deep layer (2000 m), as shown in Fig. 6, the reconstruction captures the large-scale  
 369 horizontal gradients associated with the global thermohaline circulation. The spatial distribution aligns with the general nutrient  
 370 accumulation pattern (Broecker, 1991), transitioning from the relatively nutrient-poor North Atlantic Deep Water (NADW) to  
 371 the older, nutrient-rich Pacific Deep Water (PDW) (Sarmiento and Gruber, 2006).



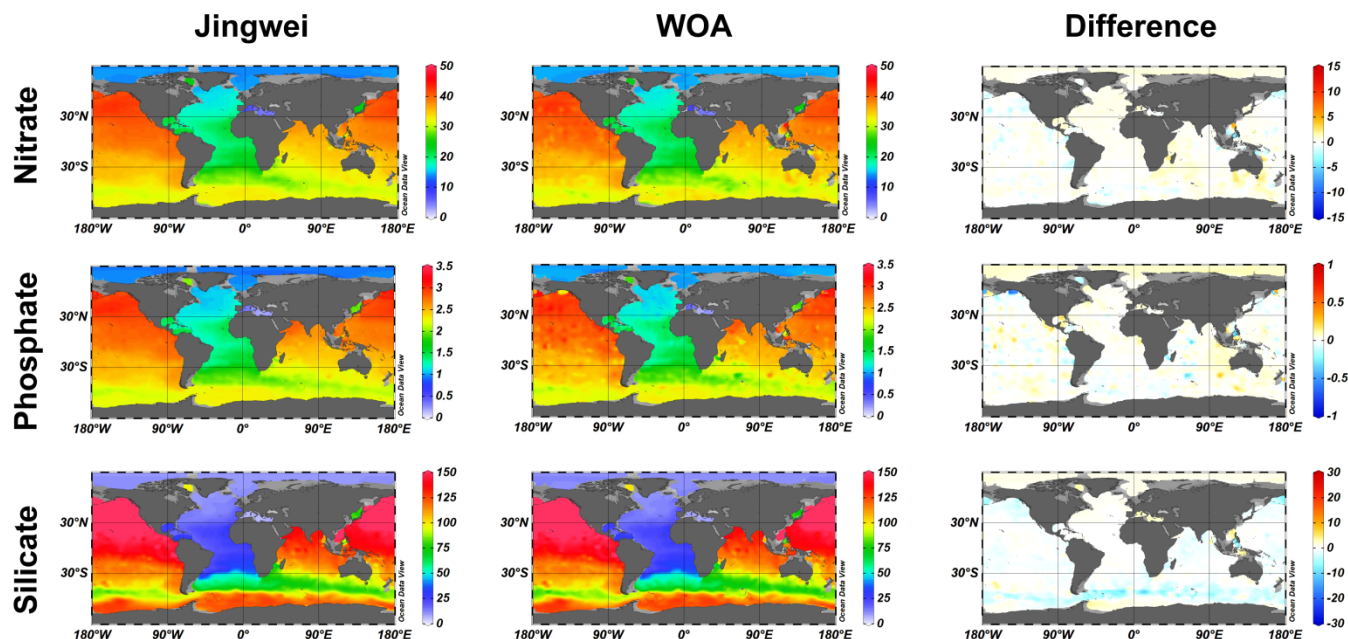
372 **Figure 4.** Spatial comparison of the climatological mean distributions of nitrate, phosphate, and silicate at the sea surface (0 m). The left  
 373 column displays the *Jingwei-Nutrients* reconstruction, the middle column shows the WOA23 standard reference, and the right column  
 374 presents the absolute difference (*Jingwei* minus WOA23). The surface fields highlight the model's precise capture of nutrient-depleted  
 375 subtropical gyres and nutrient-rich outcropping zones.



376



377 **Figure 5.** The Global climatological distributions of nitrate, phosphate, and silicate at the intermediate layer (500 m). The column and row  
378 layout is identical to Fig. 4.



379 **Figure 6.** Global climatological distributions of nitrate, phosphate, and silicate at the deep layer (2000 m). The column and row layout is  
380 identical to Fig. 4.  
381

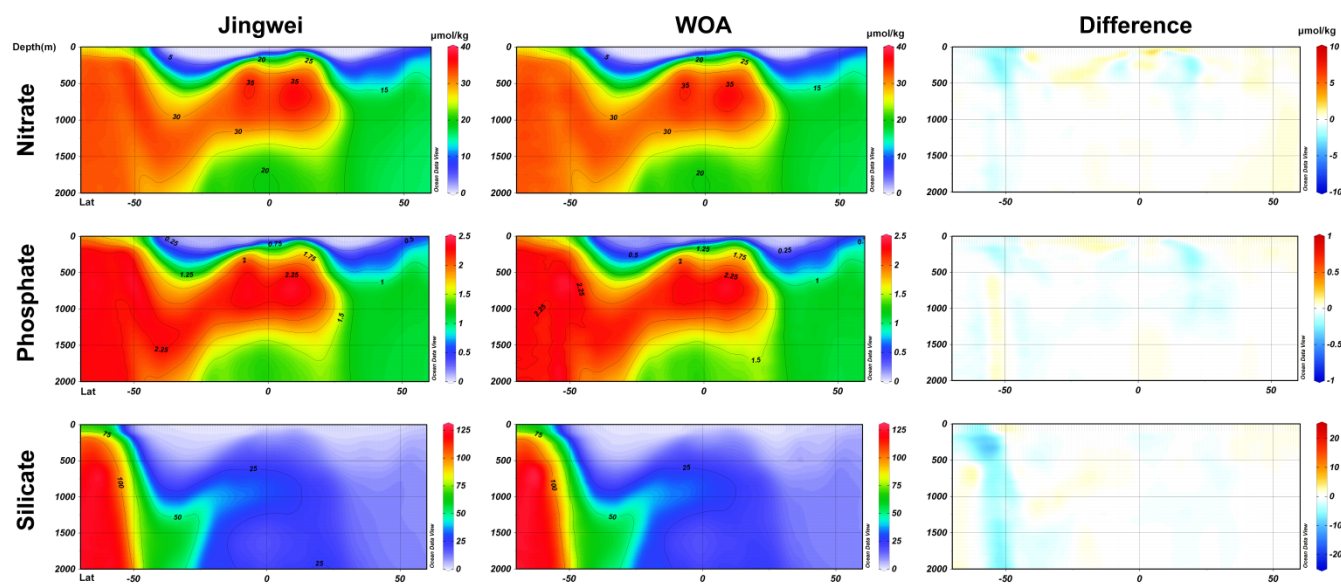
382 The difference maps between the reconstructed fields and WOA23 provide further insight into the spatial distribution of  
383 residuals. While the anomalies are generally low across open-ocean basins, their spatial and vertical distributions exhibit  
384 structured patterns. Spatially, larger deviations are primarily located in high-latitude regions (e.g., the Southern Ocean) and  
385 certain coastal margins. Vertically, the differences in the shallow euphotic layers tend to be larger than those in the deep ocean.  
386 This spatial-vertical contrast aligns with established oceanographic processes: surface waters and high-latitude regimes are  
387 modulated by seasonal biological uptake, atmospheric forcing, and mesoscale dynamics (Benitez-Nelson et al., 2007; Moore  
388 et al., 2013), introducing greater natural variability. In contrast, the deep ocean is characterized by relatively stable, slow-  
389 moving water masses driven by large-scale circulation. Overall, these regional variations are physically interpretable, and the  
390 comparison indicates that the *Jingwei-Nutrients* product provides a consistent representation of global biogeochemical  
391 distributions.

392 The vertical representation of the reconstructed fields is examined by comparing meridional sections across distinct ocean  
393 basins. Figures 7 and 8 present the vertical distributions of nitrate, phosphate, and silicate along two representative lines: 25°W  
394 in the Atlantic Ocean and 90°E in the Indian Ocean. The reconstructed fields capture the basin-scale fractionation patterns  
395 associated with the global thermohaline circulation. As illustrated in Fig. 7, the Atlantic sector exhibits relatively lower nutrient  
396 concentrations, showing the southward-intruding tongue of the ventilated, nutrient-poor North Atlantic Deep Water (NADW)

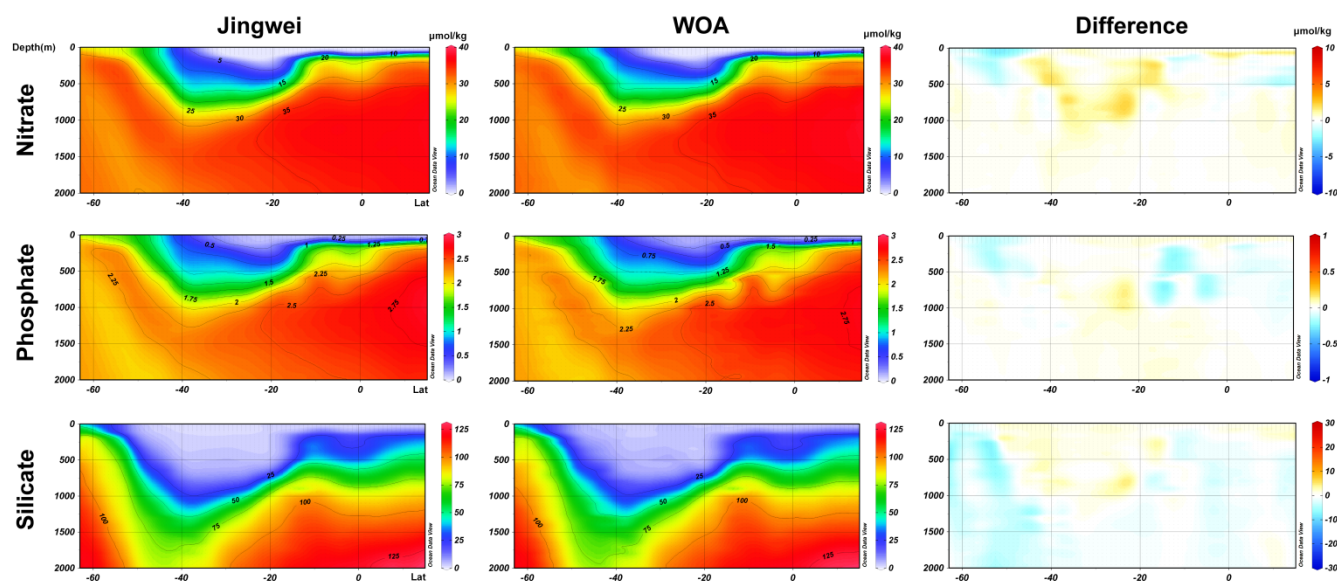


397 in the mid-to-deep layers. Conversely, Fig. 8 displays the transition to higher deep-water concentrations in the Indian Ocean  
398 interior, reflecting the accumulation of remineralized organic matter along the aging path of the deep circulation (Broecker,  
399 1991; Sarmiento and Gruber, 2006). Across both basins, the characteristic vertical gradient—rapid nutrient depletion in the  
400 euphotic zone followed by an increase across the thermocline to a deep maximum—is evident, indicating that the  
401 reconstruction captures the vertical coupling associated with the biological pump and subsequent subsurface remineralization  
402 (Sigman and Hain, 2012).

403 The difference maps in the rightmost columns of Fig. 7 and Fig. 8 provide further details on the distribution of residuals within  
404 the ocean interior. Anomalies are generally low across the majority of the water column. However, larger deviations are  
405 primarily localized along the boundaries of major water masses and in regions characterized by sharp spatial gradients. For  
406 instance, higher differences are observed around the edges of the NADW nutrient tongue and across the stratified main  
407 thermocline. This distribution of differences is physically interpretable, as these transition zones feature intense mixing and  
408 dynamic frontogenesis, introducing greater natural variability. Furthermore, the observed differences at these complex  
409 physical-biogeochemical interfaces may partially arise from distinct methodological approaches. While traditional objective  
410 analysis relies on spatial autocorrelation, the data-driven model infers nutrient concentrations through non-linear relationships  
411 with varying physical drivers. Overall, these comparisons indicate that the *Jingwei-Nutrients* dataset provides a structurally  
412 consistent representation of three-dimensional biogeochemical distributions.



413  
414 **Figure 7.** Vertical distribution of climatological mean nutrients along the 25°W meridional section in the Atlantic Ocean. The left column  
415 presents the *Jingwei-Nutrients* reconstruction, the middle column displays the WOA23 standard reference, and the right column shows the  
416 absolute difference (*Jingwei* minus WOA23). Rows from top to bottom correspond to nitrate, phosphate, and silicate, respectively. Units for  
417 all concentrations and differences are  $\mu\text{mol kg}^{-1}$ .



418

419

420

**Figure 8.** Vertical distribution of climatological mean nutrients along the 90°E meridional section in the Indian Ocean. The panel layout and represented variables are identical to those in Figure 7. Units for all concentrations and differences are  $\mu\text{mol kg}^{-1}$ .

421

422

423

424

425

426

427

428

429

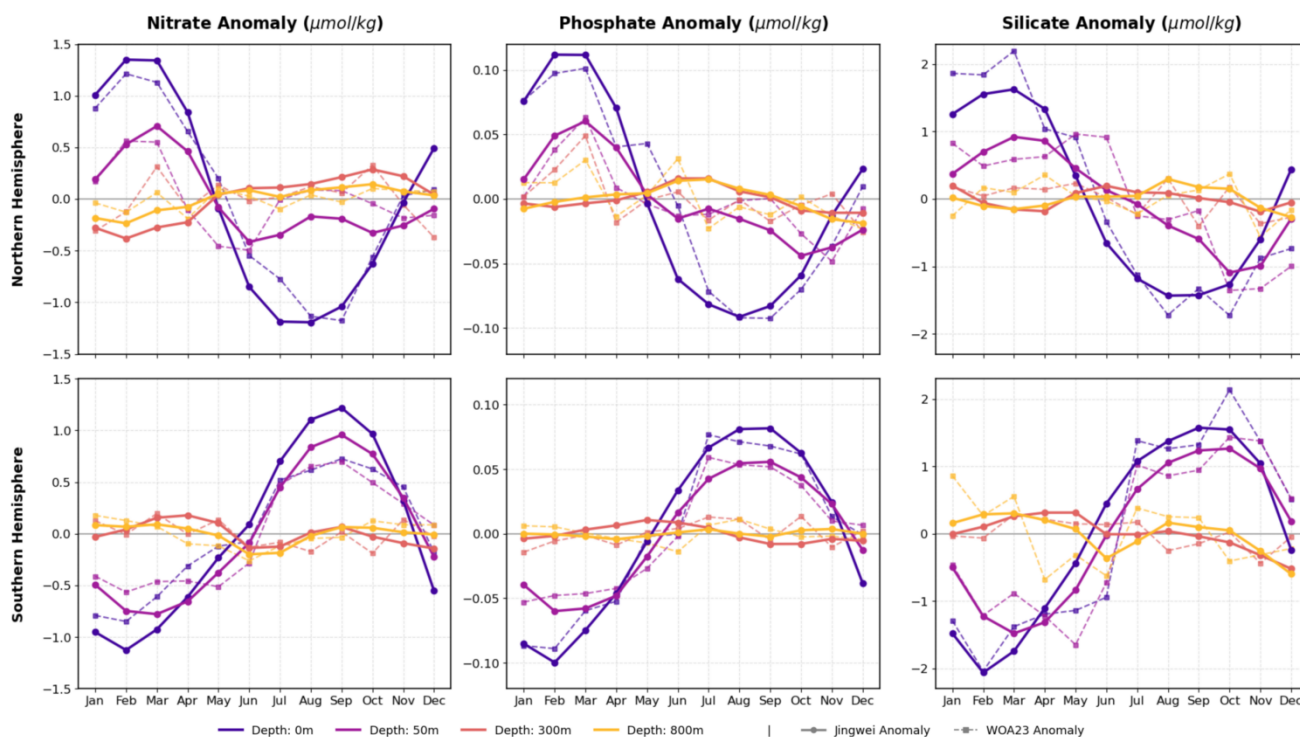
430

431

432

433

Beyond static spatial patterns, the temporal evolution of nutrient fields is critical for understanding ecosystem dynamics and phenology (Longhurst, 2007). Figure 9 compares the reconstructed seasonal anomaly cycles with WOA23 data across the Northern and Southern Hemispheres at four representative depths (0, 50, 300, and 800 m). The *Jingwei-Nutrients* reconstruction (solid lines) aligns with the WOA23 reference (dashed lines), capturing both the phase and amplitude of the seasonal variations. The model reproduces the out-of-phase seasonal dynamics between the two hemispheres. In the biologically active shallow layers (0 and 50 m), a pronounced seasonal amplitude is evident: the Northern Hemisphere shows winter/spring replenishment (Jan–Mar) mediated by convective mixing, followed by a distinct summer/autumn drawdown (Jul–Oct) driven by phytoplankton blooms (Behrenfeld et al., 2006; Keppler et al., 2020), while the Southern Hemisphere mirrors this pattern to reflect austral seasonality. Furthermore, the reconstruction captures the vertical attenuation of seasonal variability. While the euphotic zone experiences significant temporal fluctuations, the seasonal anomalies at deeper layers (300 m and 800 m) are thermodynamically and biologically dampened, maintaining stable, near-zero baseline fluctuations throughout the year (Talley, 2013). This temporal agreement indicates that the *Jingwei-Nutrients* dataset captures the phenological timing of global biogeochemical cycles.



434  
 435 **Figure 9.** Seasonal cycles of nutrient anomalies across different hemispheres and depth layers. Solid lines indicate the *Jingwei-Nutrients*  
 436 reconstruction, and dashed lines represent the WOA23 reference. The top row shows the Northern Hemisphere, and the bottom row shows  
 437 the Southern Hemisphere, encompassing nitrate, phosphate, and silicate (from left to right) at 0, 50, 300, and 800 m depths. Units are  
 438  $\mu\text{mol kg}^{-1}$ .

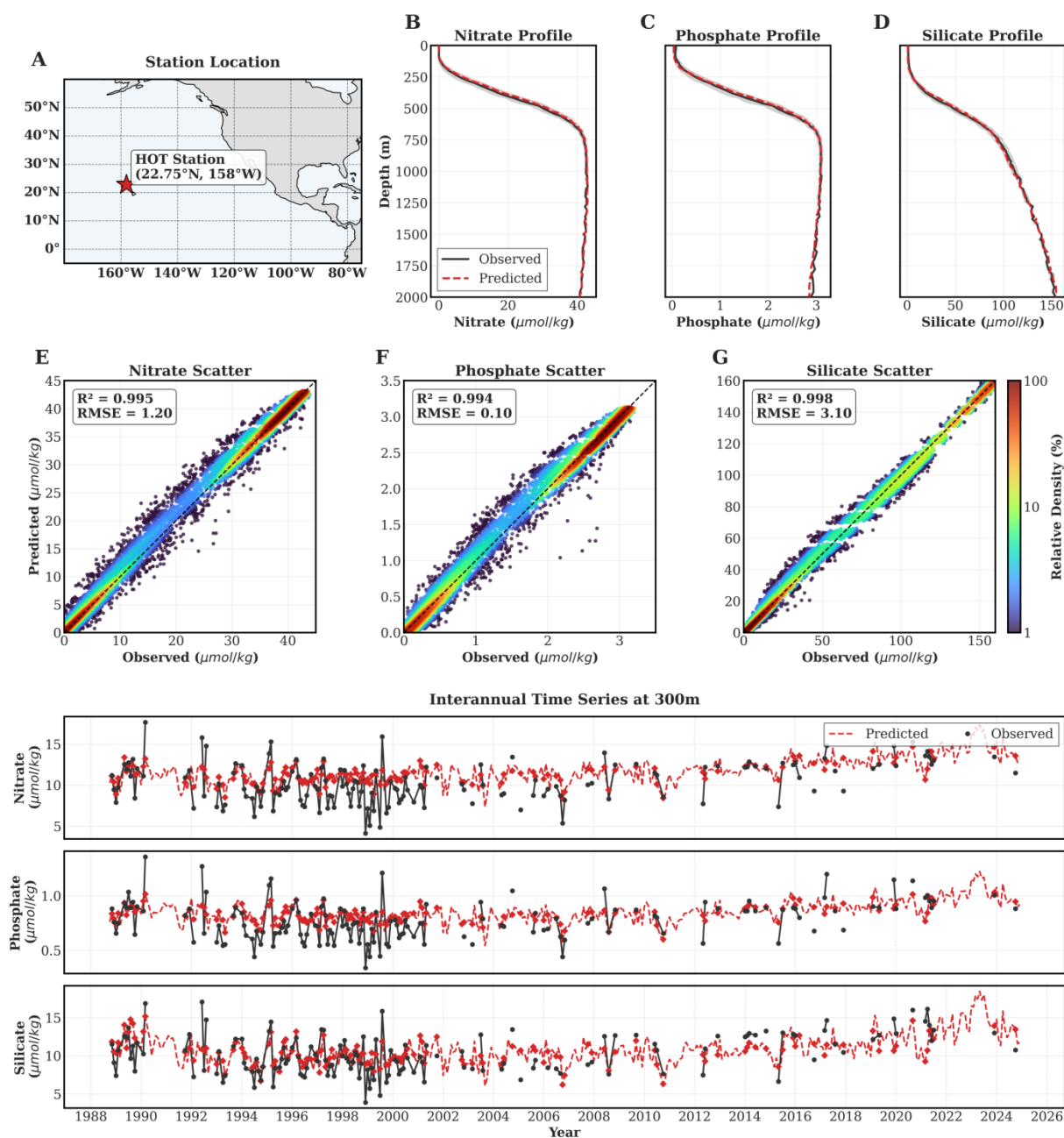
### 439 3.3 Temporal Dynamics through Station Validation

440 To assess the reproduction of localized biogeochemical variability, we perform independent validations using in situ  
 441 observations from two globally representative, long-term ecological time-series stations. These observatories encompass  
 442 distinct marine biogeochemical regimes: the Hawaii Ocean Time-series (HOT; Karl and Lukas, 1996), which represents the  
 443 highly stratified, oligotrophic subtropical gyre of the North Pacific; conversely, the KERFIX station (Jeandel et al., 1998) in  
 444 the Southern Ocean represents a dynamic, high-latitude regime dominated by deep convective winter mixing and intense  
 445 seasonal blooms.

446 Figure 10 presents the evaluations for the HOT station. The *Jingwei-Nutrients* dataset shows consistent agreement with  
 447 observations. As shown in the scatter plots, the predicted concentrations at the HOT station (Fig. 10) tightly cluster around the  
 448 1:1 reference line, yielding high localized correlation coefficients ( $R^2 \geq 0.994$ ) and low RMSE (1.20, 0.10, and  $3.10 \mu\text{mol kg}^{-1}$   
 449 for nitrate, phosphate, and silicate, respectively). The vertical profile comparisons reveal that the product delineates the depth-  
 450 dependent biogeochemical gradients, capturing the stably depleted surface layers and the depth of the deep nutricline at this  
 451 location. Furthermore, for the interannual time-series comparisons, we select depth layers characterized by abundant historical



452 observations and high biogeochemical representativeness—specifically, the 300 m layer for HOT. The temporal trajectories  
453 at this specific depth demonstrate that the reconstructed fields maintain long-term stable baselines. Notably, while the historical  
454 discrete observations occasionally exhibit localized high-frequency noise or sampling-induced spikes, the continuous  
455 reconstruction smooths these short-term variations while preserving the primary physical and biological signals.  
456 Figure 11 illustrates the validation at the KERFIX station, which represents the complex dynamics of the Southern Ocean. The  
457 time-series trajectory at the surface (0 m) indicates that the dataset captures pronounced seasonal amplitudes driven by winter  
458 overturning and subsequent summer biological drawdowns. At this station, the model yields high  $R^2$  values for nitrate  
459 ( $R^2=0.908$ ) and silicate ( $R^2=0.967$ ), indicating that it captures the complex regional water mass mixing processes, such as the  
460 upwelling of Circumpolar Deep Water (CDW) (Talley, 2013). However, a relatively lower correlation is observed for  
461 phosphate ( $R^2=0.758$ ). This specific discrepancy can be attributed to two factors. First, the absolute background concentration  
462 of surface phosphate is naturally low, which reduces the signal-to-noise ratio in historical observations and mathematically  
463 amplifies the penalty of analytical errors on the  $R^2$  metric. Second, the intense iron limitation characteristic of the Southern  
464 Ocean (Boyd et al., 2007; Moore et al., 2013) often triggers localized decoupling of the classical N:P uptake ratio (Deutsch  
465 and Weber, 2012), a highly specific regional anomaly that poses a generalization challenge for global-scale reconstructions.  
466 Nevertheless, despite the lower  $R^2$ , the absolute error for phosphate at KERFIX remains low (RMSE =  $0.13 \mu\text{mol kg}^{-1}$ ). This  
467 suggests that, even in dynamically complex and anomalous oceanic regimes, the *Jingwei-Nutrients* product provides a reliable  
468 basis for large-scale climatological and temporal analyses.  
469

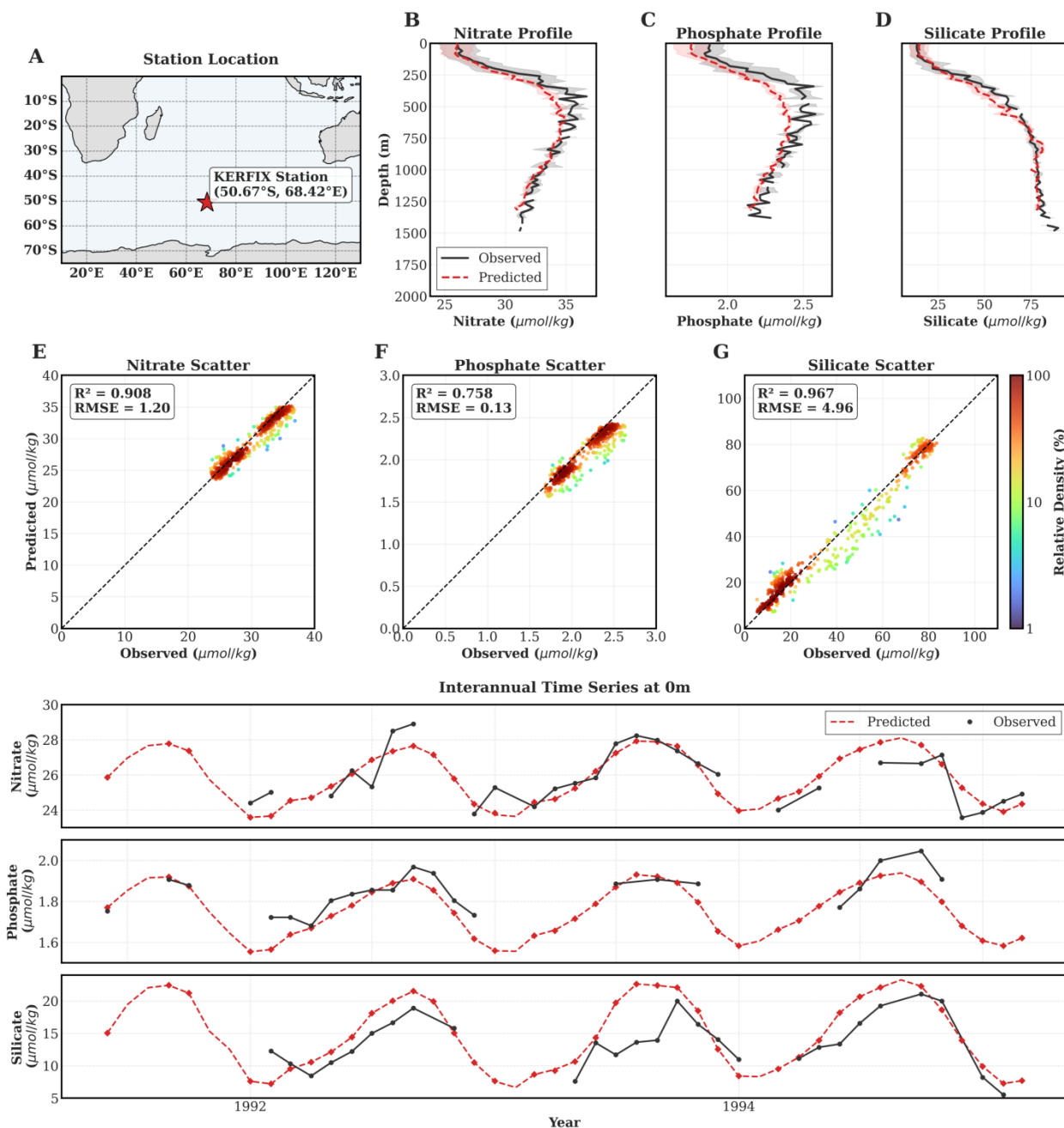


470

471 **Figure 10.** Multi-scale temporal and vertical validation at the Hawaii Ocean Time-series (HOT) station in the North Pacific. (A)  
472 Geographical location of the HOT station. (B–D) Climatological vertical profiles comparing in situ observations (black solid lines) and  
473 *Jingwei-Nutrients* predictions (red dashed lines) for nitrate, phosphate, and silicate. (E–G) Density scatter plots evaluating the overall  
474 predictive accuracy, with  $R^2$  and RMSE metrics embedded. The bottom panels display the interannual time series of nutrient concentrations  
475 evaluated at the 300 m depth layer, demonstrating the model's capability to maintain stable, long-term baselines.



476

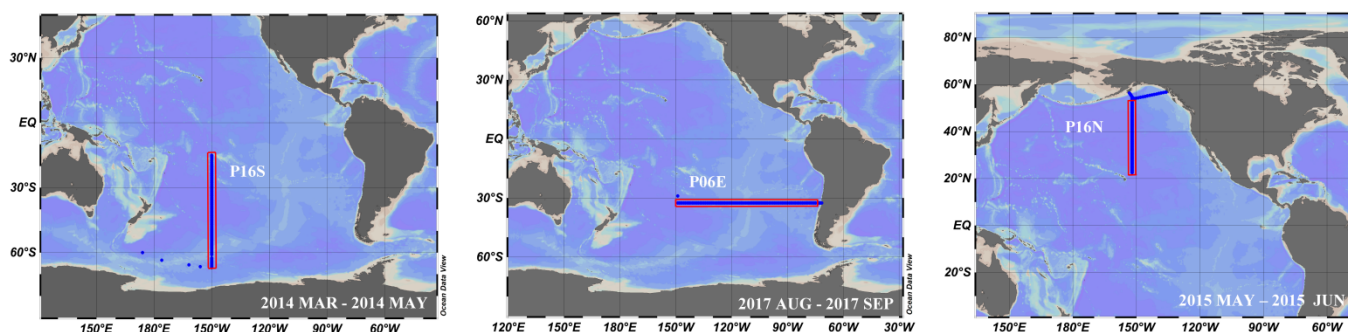


477 **Figure 11.** Multi-scale temporal and vertical validation at the KERFIX station in the Southern Ocean. The panel layout is identical to Fig.  
478 10. This figure highlights the model's performance in a highly dynamic, high-latitude regime. The interannual time series (bottom panels)  
479 are evaluated at the surface layer (0 m) to explicitly track the massive seasonal amplitudes driven by deep convective winter mixing and  
480 summer biological drawdowns.



### 481 3.4 Spatial Variability through Cruise Verification

482 Complementing the temporal validations, capturing the three-dimensional spatial variability of the ocean interior is equally  
483 critical. To assess the spatial representation of the *Jingwei-Nutrients* product, we conduct independent validations using high-  
484 resolution, synoptic shipboard measurements from the U.S. GO-SHIP program (Sloyan et al., 2019). Unlike gridded  
485 climatologies that tend to smooth out transient features, continuous cruise sections provide a "snapshot" of the product's ability  
486 to reconstruct sharp frontal zones and mesoscale variabilities. As illustrated in Fig. 12, we select three representative expedition  
487 datasets encompassing different spatial domains: the P16S (2014) and P16N (2015) cruises, which together form a nearly  
488 complete meridional corridor across the Pacific Ocean, and the P06E (2017) cruise, which provides a zonal cross-section across  
489 the South Pacific.



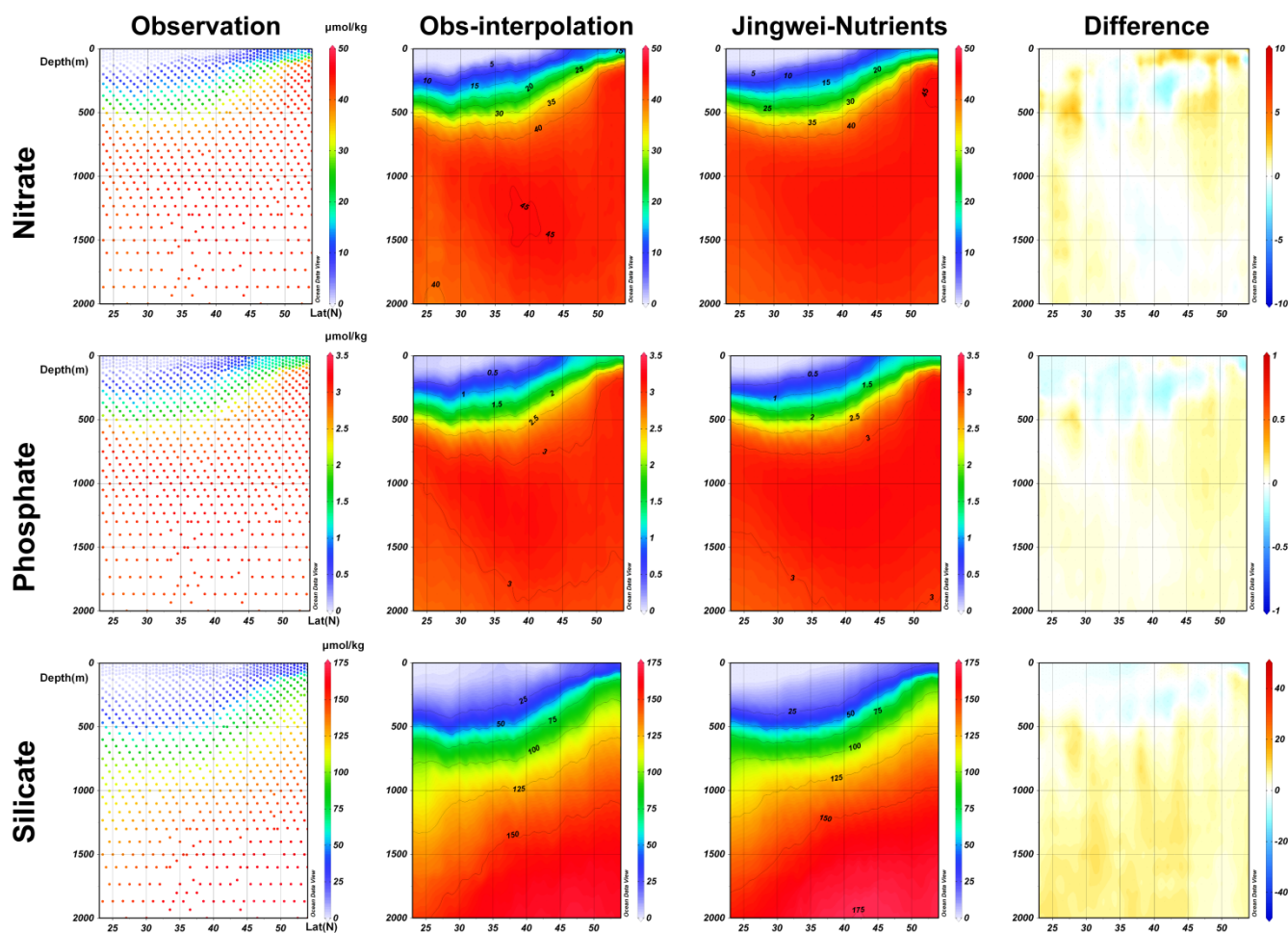
490  
491 **Figure 12.** Map of the selected U.S. GO-SHIP cruise trajectories used for independent spatial validation. The solid lines indicate the  
492 continuous high-resolution shipboard measurement sections: the P16N (2015) and P16S (2014) meridional cruises in the Pacific Ocean, and  
493 the P06E (2017) zonal cruise in the South Pacific.

494 To facilitate a direct spatial assessment, the dense in situ measurements are objectively interpolated to construct continuous  
495 observational sections. These reference fields are then compared against the coincident cross-sections extracted from the  
496 *Jingwei-Nutrients* product. Figure 13 presents the comparative contour sections and the corresponding residual error  
497 distributions for the P16N cruise in the North Pacific. The reconstructed fields reproduce the large-scale accumulation of  
498 nutrients in the deep North Pacific, exhibiting high concentrations in the deep interior. The difference maps in the rightmost  
499 column reveal that deviations for nitrate and phosphate are predominantly concentrated in the 200–500 m depth range. This  
500 depth directly coincides with the stratified main nutricline, where concentrations change rapidly over short vertical distances.  
501 For silicate along this same section, larger residuals emerge deeper in the water column below 1000 m. This specific pattern  
502 is biogeochemically consistent with the complex accumulation of dissolved silica in the oldest North Pacific Deep Water,  
503 where slow biogenic dissolution processes (Tréguer et al., 2018) contribute to larger absolute variations.

504 Moving to the Southern Hemisphere, Fig. 14 presents the validation along the P16S section. Here, the reconstruction captures  
505 the nutrient outcropping near the Southern Ocean surface. However, the difference maps reveal a distinct error structure  
506 compared to the North Pacific. A vertical band of higher anomalies spanning from the surface to the deep ocean is visible  
507 around 45°S to 50°S across all three nutrients. This localized feature corresponds to the Subantarctic Front within the Antarctic



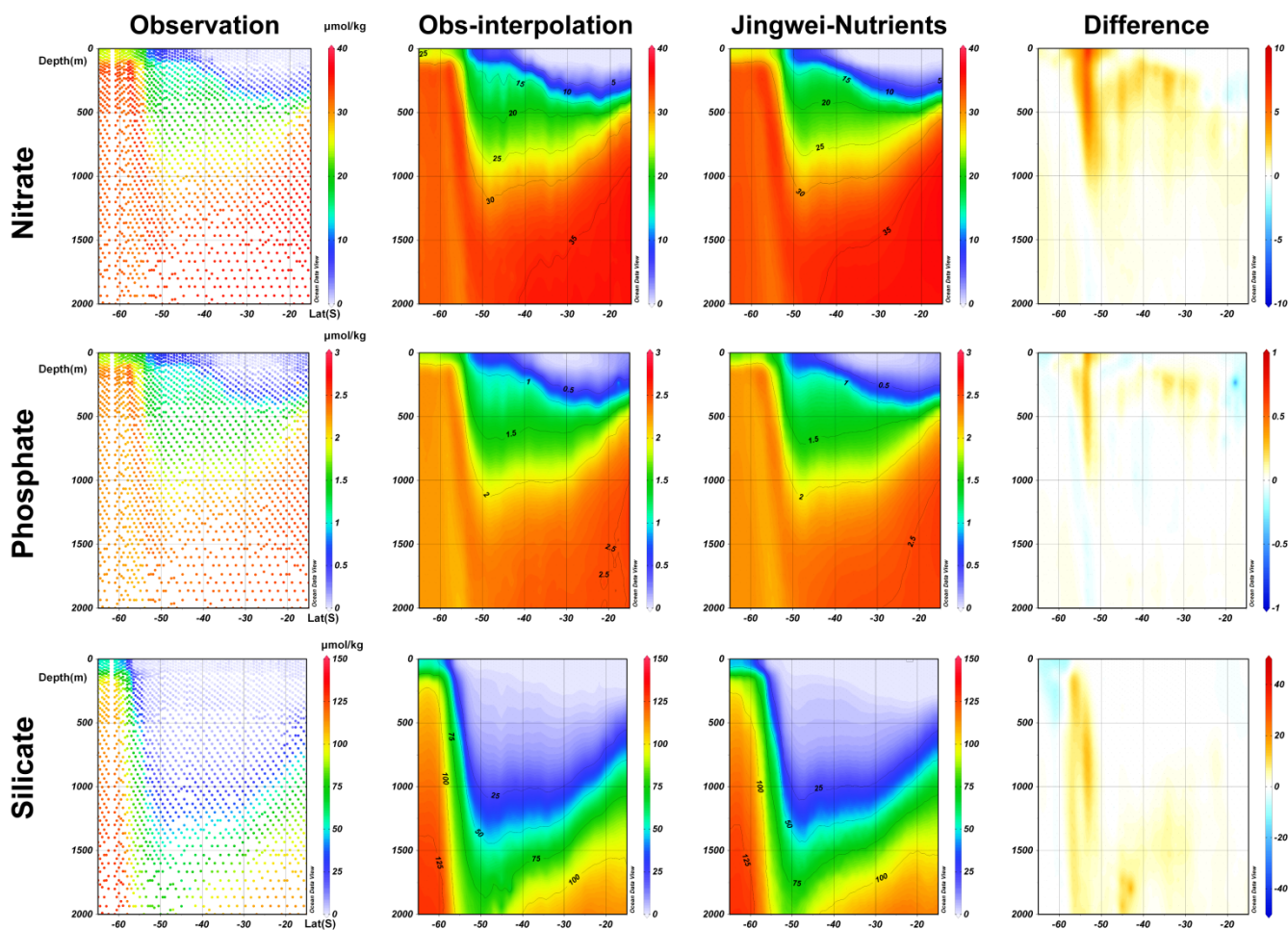
508 Circumpolar Current system. This dynamic region is characterized by energetic mesoscale eddies, intense deep vertical mixing,  
509 and steeply sloping isopycnals (Marshall and Speer, 2012), creating substantial synoptic variability in the cruise "snapshot"  
510 that naturally deviates from the temporally averaged representation of a global dataset.  
511 The zonal P06E section presented in Fig. 15 illustrates the east-west biogeochemical asymmetry across the South Pacific. The  
512 reconstructed cross-section captures the nutrient-rich upwelling signals, with concentration contours shoaling towards the  
513 South American eastern boundary, which is consistent with the cruise data. Moreover, the difference maps for this zonal section  
514 show low anomalies in the deep ocean interior, yielding minimal residuals below 1000 m across the entire basin. Deviations  
515 are primarily confined to the upper water column, driven by the coastal upwelling systems (Chavez and Messié, 2009).  
516 In summary, the cruise verification supports the three-dimensional spatial representation of the *Jingwei-Nutrients* product. By  
517 reproducing the synoptic features of these oceanographic sections across diverse dynamical regimes, the product demonstrates  
518 its capacity to reconstruct the continuous, full-depth spatial structure of global marine nutrients. The representation of deep-  
519 basin accumulations indicates that *Jingwei-Nutrients* provides a physically consistent global dataset.  
520



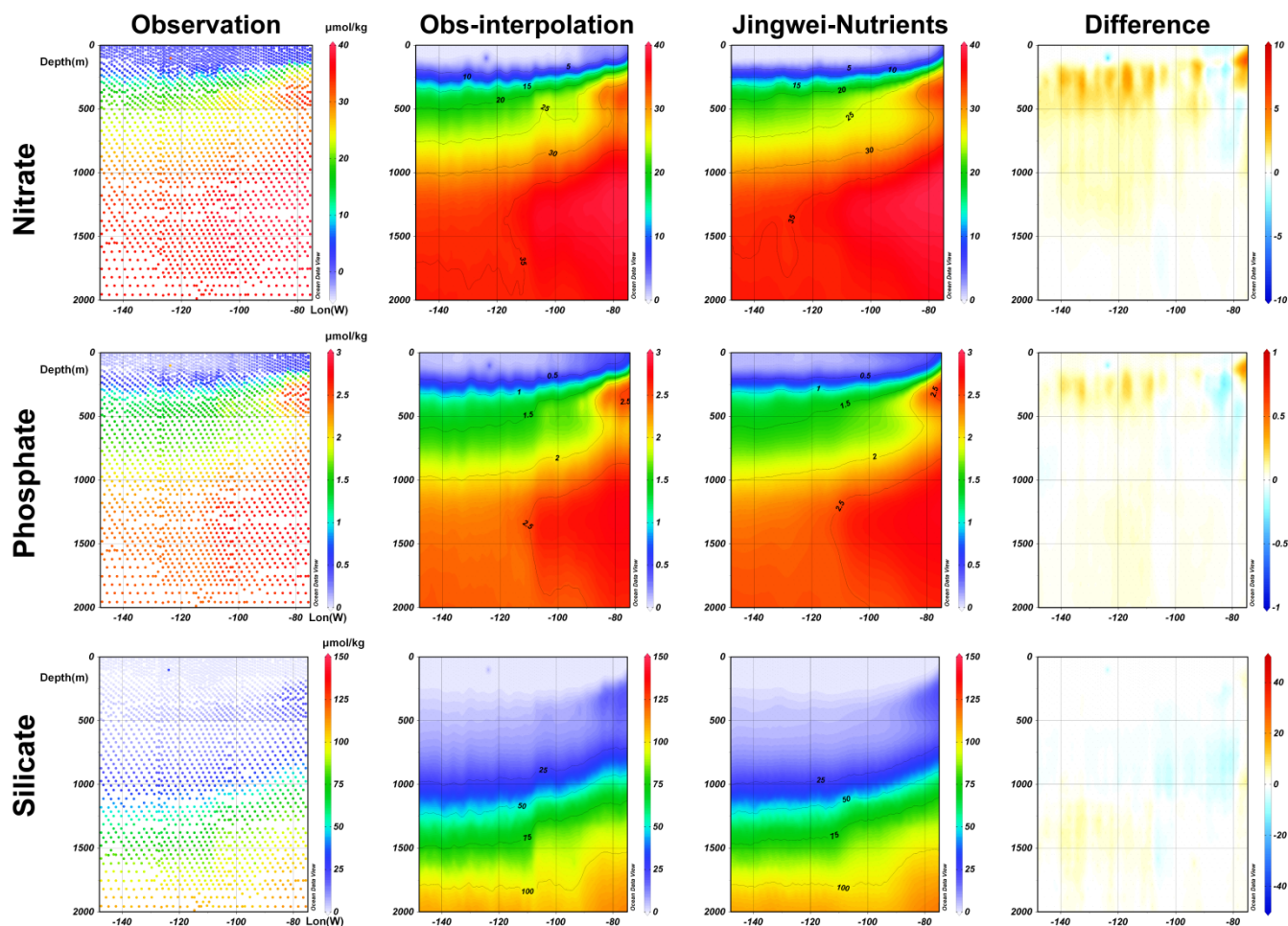
521



522 **Figure 13.** Spatial validation of nutrients along the P16N meridional section in the North Pacific. Columns from left to right display the in  
523 situ discrete shipboard measurements, the objectively interpolated observational field, the coincident cross-section extracted from the  
524 *Jingwei-Nutrients* product, and the absolute difference (*Jingwei* minus Observation). Rows from top to bottom correspond to nitrate,  
525 phosphate, and silicate, respectively.



526 **Figure 14.** Spatial validation of nutrients along the P16S meridional section in the South Pacific and Southern Ocean. The panel layout and  
527 represented variables are identical to those in Fig. 13.  
528



529

530

531

**Figure 15.** Spatial validation of nutrients along the P06E zonal section in the South Pacific. The panel layout and represented variables are identical to those in Fig. 13.

532

### 3.5 Spatiotemporal Uncertainty Analysis

533

534

535

536

537

538

To systematically evaluate the reliability of the *Jingwei-Nutrients* product, it is essential to quantify its spatiotemporal uncertainty. Since mapping sparse data often introduces more uncertainty than inherent measurement errors (Ito et al., 2025), relying solely on analytical errors is inadequate. Instead, we estimate reconstruction uncertainty using the ensemble standard deviation (std) across our six K-fold models (Gregor et al., 2019). As shown in Fig. 16, this ensemble spread remains remarkably low relative to absolute concentrations—particularly across vast open-ocean basins—confirming the high stability and reliability of the dataset.

539

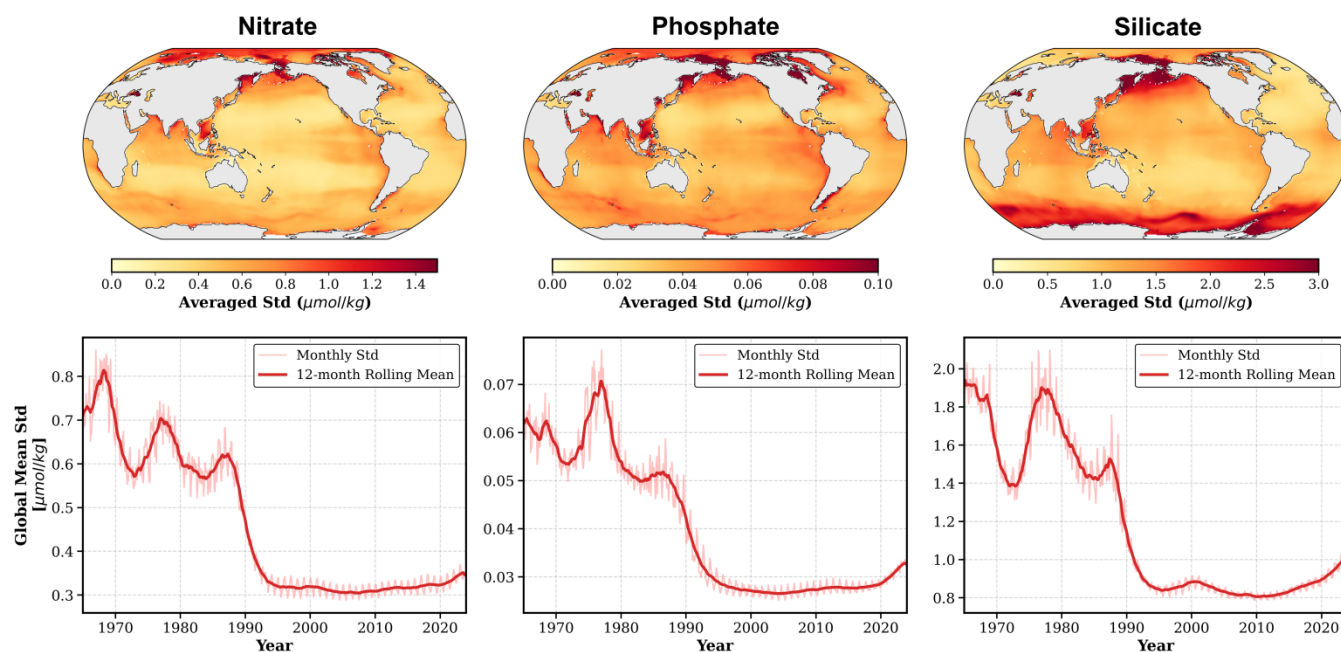
540

541

The top panels of Fig. 16 illustrate the depth-averaged spatial uncertainty for nitrate, phosphate, and silicate. The global maps reveal that the ensemble standard deviations are generally low across the open-ocean gyres, indicating model consensus in these environments. However, the uncertainty distribution exhibits spatial heterogeneities. For all three nutrients, higher



542 uncertainties are localized along coastal margins and high-latitude boundary regions. Higher uncertainty values are observed  
543 in the subpolar North Pacific—specifically within the Bering Sea and the Sea of Okhotsk. These marginal seas are  
544 characterized by shelf-basin water exchanges, riverine inputs, and seasonal phytoplankton blooms, introducing greater natural  
545 variability. Furthermore, for silicate, a band of elevated uncertainty is observed across the Southern Ocean. This is consistent  
546 with the upwelling of the Antarctic Circumpolar Current and the presence of diatom blooms, which drive biogenic silica  
547 cycling (Tréguer et al., 2018), contributing to larger absolute variations compared to nitrate and phosphate.



548 **Figure 16.** Spatiotemporal uncertainty analysis of the *Jingwei-Nutrients* reconstruction based on the ensemble standard deviation across the  
549 6-fold cross-validation models. The top row displays the spatial distribution of the depth-averaged standard deviation for nitrate, phosphate,  
550 and silicate. The bottom row presents the temporal evolution of the global mean standard deviation from 1965 to 2023. Light red lines  
551 represent the raw monthly uncertainty, while the thick red lines indicate the 12-month rolling mean.  
552

553 The bottom panels of Fig. 16 track the temporal evolution of the global mean uncertainty from 1965 to 2023. The time-series  
554 demonstrates a long-term declining trend, corresponding to the historical evolution of global ocean observing systems. A  
555 notable decrease in the global mean Std occurs around 1990. This reduction in uncertainty aligns with the onset of the World  
556 Ocean Circulation Experiment (WOCE) (Siedler et al., 2001) and the Joint Global Ocean Flux Study (JGOFS) (Fasham, 2003),  
557 which marked the transition from sparse historical sampling to systematic global hydrographic surveys.

558 Entering the 21st century, the global mean uncertainties for all three nutrients remain generally stable at lower levels compared  
559 to earlier decades. For nitrate, the deployment of the Biogeochemical-Argo (BGC-Argo) float array post-2010 (Roemmich et  
560 al., 2019; Claustre et al., 2020) provided additional autonomous profiles, contributing to the sustained low uncertainty. For  
561 phosphate and silicate, despite the gradual decline in traditional shipboard measurements in recent decades and the lack of  
562 Argo-based sensors for these elements, their mean uncertainties remain relatively low, though a slight upward trend is



563 observable in the most recent years. Ultimately, this analysis indicates that the *Jingwei-Nutrients* product provides stable  
564 reconstructions, while also highlighting the regions and periods where data sparsity introduces greater variance.

#### 565 **4 Conclusion**

566 In this study, we develop *Jingwei-Nutrients*, a global continuous dataset of ocean nutrients (nitrate, phosphate, and silicate) at  
567 a monthly resolution, spanning from 1965 to 2023. This is achieved by employing a Multi-Task Learning (MTL) Transformer  
568 architecture, trained on quality-controlled historical observations from WOD, CCHDO, GLODAP, and the BGC-Argo float  
569 array. By extracting complex nonlinear relationships between discrete nutrient samples and continuous spatiotemporal  
570 hydrographic predictors, our approach effectively transforms sparse, unevenly distributed historical measurements into a  
571 continuous four-dimensional spatiotemporal field. This reconstruction expands the available nutrient data coverage, providing  
572 a global perspective on marine biogeochemical dynamics.

573 Validations across multiple scales support the reliability of the *Jingwei-Nutrients* product. The dataset accurately reproduces  
574 the climatological spatial distributions and phenological seasonal cycles of global nutrients, demonstrating consistency with  
575 the WOA23 climatology. The continuous reconstruction also captures the sharp physical-biogeochemical gradients and  
576 structural features inherent to the ocean interior. Independent synoptic validations using high-resolution GO-SHIP cruise  
577 sections (P16N, P16S, P06E) indicate the model's capacity to resolve complex three-dimensional features, including deep-  
578 basin nutrient accumulations, boundary upwelling, and dynamic mesoscale frontal zones. Furthermore, evaluations against  
579 long-term ecological time-series stations (HOT and KERFIX) show that the reconstruction captures localized interannual  
580 baselines and smooths short-term variations while preserving primary physical and biological signals. Our spatiotemporal  
581 uncertainty analysis, derived from a 6-fold ensemble standard deviation, reveals a reduction in global reconstruction  
582 uncertainty following the WOCE/JGOFS era in the 1990s. Entering the 21st century, the uncertainty estimates continue to  
583 reflect the evolution of the global observing network.

584 Despite these advances, certain limitations remain in global-scale data-driven reconstructions. Regional uncertainties persist  
585 in dynamic marginal seas, coastal boundaries, and regions dominated by mesoscale eddies (e.g., the Subantarctic Front).  
586 Additionally, biological anomalies, such as the localized decoupling of the classical N:P uptake ratio driven by iron limitation  
587 in the Southern Ocean, pose challenges for generalized global models. Future efforts should focus on integrating higher-  
588 resolution sub-mesoscale physical forcings, assimilating emerging multi-sensor BGC-Argo data, and developing sub-regional  
589 modeling frameworks to better capture localized non-stationary biogeochemical processes.

590 The *Jingwei-Nutrients* dataset provides a physically consistent baseline of global ocean nutrients over the past six decades. It  
591 offers an observational benchmark for evaluating Earth System Models (ESMs), supports investigations into long-term  
592 biogeochemical responses to anthropogenic climate change, and serves as high-resolution boundary conditions for future  
593 marine carbon cycle and ecosystem studies.



## 594 **5 Data availability**

595 The *Jingwei-Nutrients* dataset presented in this article is openly available to the public. The reconstructed 4D global monthly  
596 fields spanning from 1965 to 2023 for nitrate, phosphate, and silicate can be accessed via Zenodo at  
597 <https://doi.org/10.5281/zenodo.19491198> (Wang et al., 2026). The dataset is provided in standard NetCDF format.

598 The primary in situ observation data used to train the data-driven non-linear models are harmonized from major public archives,  
599 including the World Ocean Database (WOD; <https://www.ncei.noaa.gov/products/world-ocean-database>; Boyer et al., 2018;  
600 Mishonov et al., 2024; Garcia et al., 2026), the Global Ocean Data Analysis Project (GLODAP; <https://doi.org/10.25921/1f4w-0t92>;  
601 Lauvset et al., 2022), the CLIVAR and Carbon Hydrographic Data Office (CCHDO; <https://cchdo.ucsd.edu>; Sloyan et  
602 al., 2019), and the Argo program (<https://doi.org/10.17882/42182>; Claustre et al., 2020). The physical driver datasets and  
603 background reference fields, specifically the EN4 hydrographic objective analyses (<https://www.metoffice.gov.uk/hadobs/en4/>;  
604 Good et al., 2013) and the World Ocean Atlas (WOA) climatologies (<https://www.ncei.noaa.gov/products/world-ocean-atlas>;  
605 Locarnini et al., 2018, 2019; Zweng et al., 2018; Reagan et al., 2019; Garcia et al., 2024a, b), are publicly available from the  
606 Met Office Hadley Centre and the NOAA National Centers for Environmental Information (NCEI), respectively.

## 607 **The Name of *Jingwei***

608 *Jingwei* is a classic figure in Chinese mythology, featured in the "Shan Hai Jing" (see <https://en.wikipedia.org/wiki/Jingwei>).  
609 The story tells of *Jingwei*, the daughter of Emperor Yan, who drowned in the East Sea. She was reborn as a bird and decided  
610 to fill the sea with pebbles and twigs, endeavoring to prevent similar tragedies. Today, *Jingwei* symbolizes perseverance and  
611 determination, embodying the spirit of never giving up despite difficult challenges.

612 This project is named *Jingwei - Nutrients* to honor the collective determination of generations of oceanographers, researchers,  
613 and vessel crews. The historical biogeochemical observations they have painstakingly collected—often scattered across vast  
614 spatial scales and decades of time—might appear as fragmented as the pebbles carried by *Jingwei*. Yet, it is through the  
615 persistent accumulation of these "pebbles" of data that we can finally reconstruct the complex patterns of global nutrient  
616 cycling. This name serves as a tribute to those who venture into the field to sense the pulse of our oceans, embodying the spirit  
617 of persistent exploration that makes global-scale synthesis possible.

## 618 **Author contributions**

619 BL, MJ, and ZW designed the study and dataset. ZW and YX collected and processed the data, developed the code, and  
620 performed the analysis. TI, LZ, LC, YL, and XW provided methodological guidance and advice. ZW wrote the original draft.  
621 All authors reviewed and edited the manuscript.



## 622 **Competing interests**

623 The contact author has declared that none of the authors has any competing interests.

## 624 **Acknowledgements**

625 This study is funded by the National Natural Science Foundation of China (Grants T2421002 and 62602003), the Postdoctoral  
626 Fellowship Program of CPSF (Grant GZB20250806), and the AI for Science Seed Program of Shanghai Jiao Tong University  
627 (Grant 2025AI4S-QY01). We extend our sincere gratitude to Dr. Jonathan D. Sharp (University of Washington  
628 CICOES/PMEL) for his valuable suggestions and insightful discussions regarding the nutrient reconstruction work. We thank  
629 the CCHDO, the WOD, GLODAP, and the BGC-Argo program for providing the observational data used in this study. Special  
630 thanks are owed to all scientists and vessel crews involved in data collection, analysis, and management for these programs.

## 631 **References**

- 632 Ascani, F., Richards, K. J., Firing, E., Grant, S., Johnson, K. S., Jia, Y., Lukas, R., and Bidigare, R. R.: Physical and biological  
633 controls of nitrate concentrations in the upper subtropical North Pacific Ocean, *Deep-Sea Res. Pt. II*, 93, 119–134,  
634 <https://doi.org/10.1016/j.dsr2.2013.01.034>, 2013.
- 635 Behrenfeld, M. J., O'Malley, R. T., Siegel, D. A., McClain, C. R., Sarmiento, J. L., Feldman, G. C., Milligan, A. J., Falkowski,  
636 P. G., Letelier, R. M., and Boss, E. S.: Climate-driven trends in contemporary ocean productivity, *Nature*, 444, 752–755,  
637 <https://doi.org/10.1038/nature05317>, 2006.
- 638 Benitez-Nelson, C. R., Bidigare, R. R., Dickey, T. D., Landry, M. R., Leonard, C. L., Brown, S. L., Nencioli, F., Rii, Y. M.,  
639 Maiti, K., Becker, J. W., Bibby, T. S., Black, W., Cai, W.-J., Carlson, C. A., Chen, F., Kuwahara, V. S., Mahaffey, C.,  
640 McAndrew, P. M., Quay, P. D., Rappé, M. S., Selph, K. E., Simmons, M. P., and Yang, E. J.: Mesoscale Eddies Drive Increased  
641 Silica Export in the Subtropical Pacific Ocean, *Science*, 316, 1017–1021, <https://doi.org/10.1126/science.1136221>, 2007.
- 642 Bi, K., Xie, L., Zhang, H., Chen, X., Gu, X., and Tian, Q.: Accurate medium-range global weather forecasting with 3D neural  
643 networks, *Nature*, 619, 533–538, <https://doi.org/10.1038/s41586-023-06185-3>, 2023.
- 644 Bittig, H. C., Steinhoff, T., Claustre, H., Fiedler, B., Williams, N. L., Sauzède, R., Körtzinger, A., and Gattuso, J.-P.: An  
645 alternative to static climatologies: Robust estimation of open ocean CO<sub>2</sub> variables and nutrient concentrations from T, S, and  
646 O<sub>2</sub> data using Bayesian neural networks, *Front. Mar. Sci.*, 5, 328, <https://doi.org/10.3389/fmars.2018.00328>, 2018.
- 647 Boyd, P. W., Jickells, T., Law, C. S., Blain, S., Boyle, E. A., Buesseler, K. O., Coale, K. H., Cullen, J. J., de Baar, H. J. W.,  
648 Follows, M., Harvey, M., Lancelot, C., Levasseur, M., Owens, N. P. J., Pollard, R., Rivkin, R. B., Sarmiento, J., Schoemann,  
649 V., Smetacek, V., Takeda, S., Tsuda, A., Turner, S., and Watson, A. J.: Mesoscale iron enrichment experiments 1993–2005:  
650 Synthesis and future directions, *Science*, 315, 612–617, <https://doi.org/10.1126/science.1131669>, 2007.



- 651 Boyer, T. P., Baranova, O. K., Coleman, C., Garcia, H. E., Grodsky, A., Locarnini, R. A., Mishonov, A. V., Paver, C. R.,  
652 Reagan, J. R., Seidov, D., Smolyar, I. V., Weathers, K., and Zweng, M. M.: World Ocean Database 2018, NOAA Atlas  
653 NESDIS 87, 2018.
- 654 Broecker, W. S.: The great ocean conveyor, *Oceanography*, 4, 79–89, <https://doi.org/10.5670/oceanog.1991.07>, 1991.
- 655 Broullón, D., Pérez, F. F., Velo, A., Hoppema, M., Olsen, A., Takahashi, T., Key, R. M., Tanhua, T., Santana-Casiano, J. M.,  
656 and Kozyr, A.: A global monthly climatology of total alkalinity: a neural network approach, *Earth Syst. Sci. Data*, 11, 1109–  
657 1127, <https://doi.org/10.5194/essd-11-1109-2019>, 2019.
- 658 Broullón, D., Pérez, F. F., Velo, A., Hoppema, M., Olafsson, J., and Ríos, A. F.: A global monthly climatology of  
659 macronutrients in the surface ocean, *Earth Syst. Sci. Data*, 13, 2593–2612, <https://doi.org/10.5194/essd-13-2593-2021>, 2021.
- 660 Browning, T. J. and Moore, C. M.: Global analysis of ocean phytoplankton nutrient limitation reveals high prevalence of co-  
661 limitation, *Nat. Commun.*, 14, 5014, <https://doi.org/10.1038/s41467-023-40774-0>, 2023.
- 662 Carter, B. R., Bittig, H. C., Fassbender, A. J., Sharp, J. D., Takeshita, Y., Xu, Y.-Y., Álvarez, M., Wanninkhof, R., Feely, R.  
663 A., and Barbero, L.: New and updated global empirical seawater property estimation routines, *Limnol. Oceanogr. Methods*,  
664 19, 785–809, <https://doi.org/10.1002/lom3.10461>, 2021.
- 665 Chavez, F. P. and Messié, M.: A comparison of eastern boundary upwelling ecosystems, *Prog. Oceanogr.*, 83, 80–96,  
666 <https://doi.org/10.1016/j.pocean.2009.07.032>, 2009.
- 667 Cheng, L., Trenberth, K. E., Fasullo, J., Boyer, T., Abraham, J., and Zhu, J.: Improved estimates of ocean heat content from  
668 1960 to 2015, *Sci. Adv.*, 3, e1601545, <https://doi.org/10.1126/sciadv.1601545>, 2017.
- 669 Claustre, H., Johnson, K. S., and Takeshita, Y.: Observing the global ocean with biogeochemical-Argo, *Annu. Rev. Mar. Sci.*,  
670 12, 23–48, <https://doi.org/10.1146/annurev-marine-010419-010956>, 2020.
- 671 Deutsch, C. and Weber, T.: Nutrient Ratios as a Tracer and Driver of Ocean Biogeochemistry, *Annu. Rev. Mar. Sci.*, 4, 113–  
672 138, <https://doi.org/10.1146/annurev-marine-120709-142821>, 2012.
- 673 Fasham, M. J. R. (Ed.): *Ocean Biogeochemistry: The Role of the Ocean Carbon Cycle in Global Change*, Springer, Berlin,  
674 Heidelberg, 324 pp., <https://doi.org/10.1007/978-3-642-55844-3>, 2003.
- 675 Garcia, H. E., Weathers, K. W., Paver, C. R., Smolyar, I. V., Boyer, T. P., Locarnini, R. A., Zweng, M. M., Mishonov, A. V.,  
676 Baranova, O. K., Seidov, D., and Reagan, J. R.: World Ocean Atlas 2018, Volume 4: Dissolved Inorganic Nutrients (phosphate,  
677 nitrate and nitrate+nitrite, silicate), NOAA Atlas NESDIS 84, 35 pp., <https://doi.org/10.25923/ng6j-ey81>, 2018.
- 678 Garcia, H. E., Bouchard, C., Cross, S. L., Paver, C. R., Wang, Z., Reagan, J. R., Boyer, T. P., Locarnini, R. A., Mishonov, A.  
679 V., Baranova, O. K., Seidov, D., and Dukhovskoy, D.: World Ocean Atlas 2023, Volume 4: Dissolved Inorganic Nutrients  
680 (Phosphate, Nitrate, and Silicate), NOAA Atlas NESDIS 92, <https://doi.org/10.25923/39qw-7j08>, 2024a.
- 681 Garcia, H. E., Wang, Z., Bouchard, C., Cross, S. L., Paver, C. R., Reagan, J. R., Boyer, T. P., Locarnini, R. A., Mishonov, A.  
682 V., Baranova, O. K., Seidov, D., and Dukhovskoy, D.: World Ocean Atlas 2023, Volume 3: Dissolved Oxygen, Apparent  
683 Oxygen Utilization, and Oxygen Saturation, NOAA Atlas NESDIS 91, <https://doi.org/10.25923/rb67-ns53>, 2024b.



- 684 Garcia, H. E., Boyer, T. P., Levitus, S., Reagan, J. R., Mishonov, A. V., Jiang, L.-Q., Wang, Z., Paver, C. R., Nyadjro, E.,  
685 Cross, S., Bouchard, C., Hogan, P., Baranova, O. K., and Locarnini, R. A.: World Ocean Database 2023: A foundational data  
686 resource for and by the global ocean and coastal communities, *Sci. Data*, 13, 613, [https://doi.org/10.1038/s41597-026-06957-](https://doi.org/10.1038/s41597-026-06957-2)  
687 [2](https://doi.org/10.1038/s41597-026-06957-2), 2026.
- 688 Good, S. A., Martin, M. J., and Rayner, N. A.: EN4: Quality controlled ocean temperature and salinity profiles and monthly  
689 objective analyses with uncertainty estimates, *J. Geophys. Res. Oceans*, 118, 6704–6716,  
690 <https://doi.org/10.1002/2013JC009067>, 2013.
- 691 Gouretski, V. and Reseghetti, F.: On depth and temperature biases in bathythermograph data: Development of a new correction  
692 scheme based on analysis of a global ocean database, *Deep-Sea Res. Pt. I*, 57, 812–833,  
693 <https://doi.org/10.1016/j.dsr.2010.03.011>, 2010.
- 694 Gregor, L., Lebehot, A. D., Kok, S., and Scheel Monteiro, P. M.: A comparative assessment of the uncertainties of global  
695 surface ocean CO<sub>2</sub> estimates using a machine-learning ensemble (CSIR-ML6 version 2019a) – have we hit the wall?, *Geosci.*  
696 *Model Dev.*, 12, 5113–5136, <https://doi.org/10.5194/gmd-12-5113-2019>, 2019.
- 697 Ito, T., Minobe, S., Long, M. C., and Deutsch, C.: Upper ocean O<sub>2</sub> trends: 1958–2015, *Geophys. Res. Lett.*, 44, 4214–4223,  
698 <https://doi.org/10.1002/2017GL073613>, 2017.
- 699 Ito, T., Cervania, A., Cross, K., Ainchwar, S., and Delawalla, S.: Mapping dissolved oxygen concentrations by combining  
700 shipboard and Argo observations using machine learning algorithms, *J. Geophys. Res. Mach. Learn. Comput.*, 1,  
701 e2024JH000272, <https://doi.org/10.1029/2024JH000272>, 2024.
- 702 Ito, T., Garcia, H. E., Wang, Z., Cheng, L., Du, J., Roach, C. J., Zhou, Y., Sharp, J. D., Lauvset, S. K., Minobe, S., Bushinsky,  
703 S., Lu, B., and Navarra, G.: Assessing the observational uncertainties of dissolved oxygen climatology and seasonal cycle  
704 through a coordinated intercomparison project, *Global Biogeochem. Cy.*, <https://doi.org/10.1029/2025GB008751>, 2025.
- 705 Jeandel, C., Ruiz-Pino, D., Gasser, B., Etcheber, H., Brunet, C., Poisson, A., and Cronis, S.: KERFIX, a time-series station in  
706 the Southern Ocean: a presentation, *J. Marine Syst.*, 17, 555–569, [https://doi.org/10.1016/S0924-7963\(98\)00064-5](https://doi.org/10.1016/S0924-7963(98)00064-5), 1998.
- 707 Karl, D. M. and Lukas, R.: The Hawaii Ocean Time-series (HOT) program: Background, rationale and implementation, *Deep-*  
708 *Sea Res. Pt. II*, 43, 129–156, [https://doi.org/10.1016/0967-0645\(96\)00005-7](https://doi.org/10.1016/0967-0645(96)00005-7), 1996.
- 709 Kendall, A., Gal, Y., and Cipolla, R.: Multi-Task Learning Using Uncertainty to Weigh Losses for Scene Geometry and  
710 Semantics, in: *Proceedings of the IEEE Conference on Computer Vision and Pattern Recognition (CVPR)*, 7482–7491,  
711 <https://doi.org/10.1109/CVPR.2018.00781>, 2018.
- 712 Keppler, L., Landschützer, P., Gruber, N., Lauvset, S. K., and Stemmler, I.: Seasonal carbon dynamics in the near-global ocean,  
713 *Global Biogeochem. Cy.*, 34, e2020GB006571, <https://doi.org/10.1029/2020GB006571>, 2020.
- 714 Lam, R., Sanchez-Gonzalez, A., Willson, M., Wirnsberger, P., Fortunato, M., Alet, F., Ravuri, S., Ewalds, T., Eaton-Rosen,  
715 Z., Hu, W., Merose, A., Hoyer, S., Holland, G., Vinyals, O., Stott, J., Pritzel, A., Mohamed, S., and Battaglia, P.: Learning  
716 skillful medium-range global weather forecasting, *Science*, 382, 1416–1421, <https://doi.org/10.1126/science.adi2336>, 2023.



- 717 Landschützer, P., Gruber, N., and Bakker, D. C. E.: Decadal variations and trends of the global ocean carbon sink, *Global*  
718 *Biogeochem. Cy.*, 30, 1396–1417, <https://doi.org/10.1002/2015GB005359>, 2016.
- 719 Lauvset, S. K., Lange, N., Tanhua, T., Bittig, H. C., Olsen, A., Kozyr, A., Alin, S., Álvarez, M., Azetsu-Scott, K., Barbero, L.,  
720 Becker, S., Brown, P. J., Carter, B. R., da Cunha, L. C., Feely, R. A., Hoppema, M., Humphreys, M. P., Ishii, M., Jeansson,  
721 E., Jiang, L.-Q., Jones, S. D., Lo Monaco, C., Murata, A., Müller, J. D., Pérez, F. F., Pfeil, B., Schirnick, C., Steinfeldt, R.,  
722 Suzuki, T., Tilbrook, B., Ulfso, A., Velo, A., Wanninkhof, R., and Woosley, R. J.: GLODAPv2.2022: the latest version of  
723 the global interior ocean biogeochemical data product, *Earth Syst. Sci. Data*, 14, 5543–5572, [https://doi.org/10.5194/essd-14-](https://doi.org/10.5194/essd-14-5543-2022)  
724 [5543-2022](https://doi.org/10.5194/essd-14-5543-2022), 2022.
- 725 Levitus, S.: *Climatological Atlas of the World Ocean*, NOAA Professional Paper 13, US Government Printing Office,  
726 Washington, D.C., 173 pp., 1982.
- 727 Lipschultz, F., Bates, N. R., Carlson, C. A., and Hansell, D. A.: New production in the Sargasso Sea: History and current status,  
728 *Global Biogeochem. Cy.*, 16, 1001, <https://doi.org/10.1029/2000GB001319>, 2002.
- 729 Liu, J., Wang, H., Mou, J., Peñuelas, J., Delgado-Baquerizo, M., Martiny, A. C., Zhou, G., Hutchins, D. A., Inomura, K.,  
730 Lomas, M. W., Fakhraee, M., Pellegrini, A., Kohler, T. J., Deutsch, C. A., Planavsky, N., Lapointe, B., Zhang, Y., Li, Y.,  
731 Zhou, J., Zhang, Y., Sun, S., Li, Y., Zhang, W., Cao, J., and Chen, J.: Global-scale shifts in marine ecological stoichiometry  
732 over the past 50 years, *Nat. Geosci.*, 18, 769–778, <https://doi.org/10.1038/s41561-025-01735-y>, 2025.
- 733 Locarnini, R. A., Mishonov, A. V., Baranova, O. K., Boyer, T. P., Zweng, M. M., Garcia, H. E., Reagan, J. R., Seidov, D.,  
734 Weathers, K., Paver, C. R., and Smolyar, I.: *World Ocean Atlas 2018, Volume 1: Temperature*, NOAA Atlas NESDIS 81, 52  
735 pp., <https://doi.org/10.25923/e5rn-9711>, 2018.
- 736 Locarnini, R. A., Boyer, T. P., Mishonov, A. V., Reagan, J. R., Zweng, M. M., Baranova, O. K., Garcia, H. E., Seidov, D.,  
737 Weathers, K. W., Paver, C. R., and Smolyar, I. V.: *World Ocean Atlas 2018, Volume 5: Density*, NOAA Atlas NESDIS 85,  
738 41 pp., <https://doi.org/10.25923/xnf9-9s53>, 2019.
- 739 Longhurst, A. R.: *Ecological Geography of the Sea*, 2nd Edn., Academic Press, Burlington, MA, 542 pp.,  
740 <https://doi.org/10.1016/B978-0-12-455521-1.X5000-1>, 2007.
- 741 Lu, B., Zhao, Z., Han, L., Gan, X., Zhou, Y., Zhou, L., Fu, L., Wang, X., Zhou, C., and Zhang, J.: OxyGenerator:  
742 Reconstructing global ocean deoxygenation over a century with deep learning, in: *Proceedings of the 41st International*  
743 *Conference on Machine Learning*, 2024.
- 744 Marshall, J. and Speer, K.: Closure of the meridional overturning circulation through Southern Ocean upwelling, *Nat. Geosci.*,  
745 5, 171–180, <https://doi.org/10.1038/ngeo1391>, 2012.
- 746 Mishonov, A. V., Boyer, T. P., Baranova, O. K., Bouchard, C. N., Cross, S., Garcia, H. E., Locarnini, R. A., Paver, C. R.,  
747 Reagan, J. R., Wang, Z., Seidov, D., Grodsky, A. I., and Beauchamp, J. G.: *World Ocean Database 2023*, NOAA Atlas NESDIS  
748 97, 206 pp., <https://doi.org/10.25923/z885-h264>, 2024.
- 749 Moore, C. M., Mills, M. M., Arrigo, K. R., Berman-Frank, I., Bopp, L., Boyd, P. W., Galbraith, E. D., Geider, R. J., Guieu,  
750 C., Jaccard, S. L., Jickells, T. D., Lenton, T. M., Mahowald, N. M., Marañón, E., Marinov, I., Moore, J. K., Nakatsuka, T.,



- 751 Oeschlies, A., Saito, M. A., Thingstad, T., Tsuda, A., and Ulloa, O.: Processes and patterns of oceanic nutrient limitation, *Nat.*  
752 *Geosci.*, 6, 701–710, <https://doi.org/10.1038/ngeo1765>, 2013.
- 753 Olsen, A., Key, R. M., van Heuven, S., Lauvset, S. K., Velo, A., Lin, X., Schirnick, C., Kozyr, A., Tanhua, T., Hoppema, M.,  
754 Jutterström, S., Steinfeldt, R., Jeansson, E., Ishii, M., Pérez, F. F., and Suzuki, T.: The Global Ocean Data Analysis Project  
755 version 2 (GLODAPv2) – an internally consistent data product for the world ocean, *Earth Syst. Sci. Data*, 8, 297–323,  
756 <https://doi.org/10.5194/essd-8-297-2016>, 2016.
- 757 Paulmier, A. and Ruiz-Pino, D.: Oxygen minimum zones (OMZs) in the modern ocean, *Prog. Oceanogr.*, 80, 113–128,  
758 <https://doi.org/10.1016/j.pocean.2008.08.001>, 2009.
- 759 Reagan, J. R., Zweng, M. M., Seidov, D., Boyer, T. P., Locarnini, R. A., Mishonov, A. V., Baranova, O. K., Garcia, H. E.,  
760 Weathers, K. W., Paver, C. R., Smolyar, I. V., and Tyler, R. H.: World Ocean Atlas 2018, Volume 6: Conductivity, NOAA  
761 Atlas NESDIS 86, 38 pp., 2019.
- 762 Redfield, A. C.: On the proportions of organic derivatives in sea water and their relation to the composition of plankton, in:  
763 James Johnstone Memorial Volume, edited by: Daniel, R. J., University Press of Liverpool, Liverpool, 176–192, 1934.
- 764 Reichstein, M., Camps-Valls, G., Stevens, B., Jung, M., Denzler, J., Carvalhais, N., and Prabhat: Deep learning and process  
765 understanding for data-driven Earth system science, *Nature*, 566, 195–204, <https://doi.org/10.1038/s41586-019-0912-1>, 2019.
- 766 Roemmich, D., Alford, M. H., Claustre, H., Johnson, K., King, B., Moum, J., Oke, P., Owens, W. B., Pouliquen, S., Purkey,  
767 S., Scanderbeg, M., Suga, T., Wijffels, S., Zilberman, N., Bakker, D., Baringer, M., Belbeoch, M., Bittig, H. C., Boss, E., Calil,  
768 P., Carse, F., Carval, T., Chai, F., Conchubhair, D. Ó., d'Ortenzio, F., Dall'Olmo, G., Desbruyeres, D., Fennel, K., Fer, I.,  
769 Ferrari, R., Forget, G., Freeland, H., Fujiki, T., Gehlen, M., Greenan, B., Hallberg, R., Hibiya, T., Hosoda, S., Jayne, S.,  
770 Jochum, M., Johnson, G. C., Kang, K., Kolodziejczyk, N., Körtzinger, A., Le Traon, P.-Y., Lenn, Y.-D., Maze, G., Mork, K.  
771 A., Morris, T., Nagai, T., Nash, J., Naveira Garabato, A., Olsen, A., Pattabhi, R. R., Prakash, S., Riser, S., Schmechtig, C.,  
772 Schmid, C., Shroyer, E., Sterl, A., Sutton, P., Talley, L., Tanhua, T., Thierry, V., Thomalla, S., Toole, J., Troisi, A., Trull, T.  
773 W., Turton, J., Velez-Belchi, P. J., Walczowski, W., Wang, H., Wanninkhof, R., Waterhouse, A. F., Waterman, S., Watson,  
774 A., Wilson, C., Wong, A. P. S., Xu, J., and Yasuda, I.: On the Future of Argo: A Global, Full-Depth, Multi-Disciplinary Array,  
775 *Front. Mar. Sci.*, 6, 439, <https://doi.org/10.3389/fmars.2019.00439>, 2019.
- 776 Sarmiento, J. L. and Gruber, N.: *Ocean Biogeochemical Dynamics*, Princeton University Press, Princeton, NJ, 526 pp.,  
777 <https://doi.org/10.1515/9781400849079>, 2006.
- 778 Sauzède, R., Bittig, H. C., Claustre, H., Pasqueron de Fommervault, O., Gattuso, J.-P., Legendre, L., and Johnson, K. S.:  
779 Estimates of water-column nutrient concentrations and carbonate system parameters in the global ocean: A novel approach  
780 based on neural networks, *Frontiers in Marine Science*, 4, 128, <https://doi.org/10.3389/fmars.2017.00128>, 2017.
- 781 Siedler, G., Church, J., and Gould, J. (Eds.): *Ocean Circulation and Climate: Observing and Modelling the Global Ocean*,  
782 Academic Press, San Diego, CA, 716 pp., [https://doi.org/10.1016/S0074-6142\(01\)X8034-0](https://doi.org/10.1016/S0074-6142(01)X8034-0), 2001.
- 783 Sigman, D. M. and Hain, M. P.: The Biological Productivity of the Ocean, *Nat. Educ. Knowl.*, 3, 21,  
784 <https://www.nature.com/scitable/knowledge/library/the-biological-productivity-of-the-ocean-70631104/>, 2012.



- 785 Sloyan, B. M., Wanninkhof, R., Kramp, M., Johnson, G. C., Talley, L. D., Tanhua, T., McDonagh, E., Cusack, C., O'Rourke,  
786 E., McGovern, E., Katsumata, K., Diggs, S., Hummon, J., Ishii, M., Azetsu-Scott, K., Boss, E., Anson, I., Perez, F. F.,  
787 Mercier, H., Williams, M. J. M., Anderson, L., Lee, J. H., Murata, A., Kouketsu, S., Jeansson, E., Hoppema, M., and Campos,  
788 E.: The Global Ocean Ship-Based Hydrographic Investigations Program (GO-SHIP): A Platform for Integrated  
789 Multidisciplinary Ocean Science, *Front. Mar. Sci.*, 6, 445, <https://doi.org/10.3389/fmars.2019.00445>, 2019.
- 790 Sonnewald, M., Lguensat, R., Jones, D. C., Dueben, P. D., Brajard, J., and Balaji, V.: Bridging observations, theory and  
791 numerical simulation of the ocean using machine learning, *Environ. Res. Lett.*, 16, 073008, <https://doi.org/10.1088/1748-9326/ac0eb0>, 2021.
- 793 Talley, L. D.: Closure of the global overturning circulation through the Indian, Pacific, and Southern Oceans: Schematics and  
794 transports, *Oceanography*, 26, 80–97, <https://doi.org/10.5670/oceanog.2013.07>, 2013.
- 795 Tréguer, P., Bowler, C., Moriceau, B., Dutkiewicz, S., Gehlen, M., Aumont, O., Bittner, L., Dugdale, R., Finkel, Z., Iudicone,  
796 D., Jahn, O., Guidi, L., Lasbleiz, M., Leblanc, K., Levy, M., and Pondaven, P.: Influence of diatom diversity on the ocean  
797 biological carbon pump, *Nat. Geosci.*, 11, 27–37, <https://doi.org/10.1038/s41561-017-0028-x>, 2018.
- 798 Vandenhende, S., Georgoulis, S., Van Gansbeke, W., Proesmans, M., Dai, D., and Van Gool, L.: Multi-task learning for dense  
799 prediction tasks: A survey, *IEEE Trans. Pattern Anal. Mach. Intell.*, 44, 3614–3633,  
800 <https://doi.org/10.1109/TPAMI.2021.3054719>, 2022.
- 801 Vaswani, A., Shazeer, N., Parmar, N., Uszkoreit, J., Jones, L., Gomez, A. N., Kaiser, Ł., and Polosukhin, I.: Attention Is All  
802 You Need, in: *Advances in Neural Information Processing Systems*, 30, 5998–6008,  
803 <https://doi.org/10.48550/arXiv.1706.03762>, 2017.
- 804 Wang, Z., Lu, B., Xin, Y., Ito, T., Zhou, L., Cheng, L., Li, Y., Wang, X., Zhou, C., and Jin, M.: Jingwei-Nutrients: A global  
805 spatiotemporal reconstruction of ocean nutrients (1965–2023) using multi-task deep learning, Zenodo [data set],  
806 <https://doi.org/10.5281/zenodo.19491198>, 2026.
- 807 Yu, T., Kumar, S., Gupta, A., Levine, S., Hausman, K., and Finn, C.: Gradient Surgery for Multi-Task Learning, in: *Advances*  
808 *in Neural Information Processing Systems*, 33, 5824–5836, <https://doi.org/10.48550/arXiv.2001.06782>, 2020.
- 809 Zanna, L., Khatiwala, S., Gregory, J. M., Ison, J., and Heimbach, P.: Global reconstruction of historical ocean heat storage and  
810 transport, *Proc. Natl. Acad. Sci. U.S.A.*, 116, 1126–1131, <https://doi.org/10.1073/pnas.1808838115>, 2019.
- 811 Zweng, M. M., Reagan, J. R., Seidov, D., Boyer, T. P., Locarnini, R. A., Garcia, H. E., Mishonov, A. V., Baranova, O. K.,  
812 Weathers, K., Paver, C. R., and Smolyar, I.: World Ocean Atlas 2018, Volume 2: Salinity, NOAA Atlas NESDIS 82, 50 pp.,  
813 <https://doi.org/10.25923/9pgv-1224>, 2018.